ZFIRE: 3D Modeling of Rotation, Dispersion, and Angular Momentum of Star-forming Galaxies at z~2

Alcorn, L.Y.; Tran, K.V.; Glazebrook, K.; Straatman, C.M.; Cowley, M.; Forrest, B.; ... ; Yuan, T.

Draft version April 12, 2018
Typeset using LaTeX **preprint2** style in AASTeX62

ZFIRE: 3D Modeling of Rotation, Dispersion, and Angular Momentum of Star-Forming Galaxies at $z \sim 2$

Leo Y. Alcorn,[1,2,3] Kim-Vy Tran,[1,2,4] Karl Glazebrook,[5] Caroline M. Straatman,[6] Michael Cowley,[7,8] Ben Forrest,[1,2] Glenn G. Kacprzak,[5] Lisa J. Kewley,[9] Ivo Labbé,[5,10] Themiya Nanayakkara,[5,10] Lee R. Spitler,[7,8] Adam Tomczak,[11] and Tiantian Yuan[5]

[1]*Department of Physics and Astronomy, Texas A&M University, College Station, TX, 77843-4242 USA*
[2]*George P. and Cynthia Woods Mitchell Institute for Fundamental Physics and Astronomy, Texas A&M University, College Station, TX, 77843-4242*
[3]*LSSTC Data Science Fellow*
[4]*School of Physics, University of New South Wales, Sydney, NSW 2052, Australia*
[5]*Swinburne University of Technology, Hawthorn, VIC 3122, Australia*
[6]*Max Planck Institut für Astronomie, Königstuhl 17, 69117 Heidelberg, Germany*
[7]*Australian Astronomical Observatory, PO Box 915, North Ryde, NSW 1670, Australia*
[8]*Department of Physics and Astronomy, Faculty of Science and Engineering, Macquarie University, Sydney, NSW 2109, Australia*
[9]*Research School of Astronomy and Astrophysics, The Australian National University, Cotter Road, Weston Creek, ACT 2611, Australia*
[10]*Leiden Observatory, Leiden University, P.O. Box 9513, NL 2300 RA Leiden, The Netherlands*
[11]*Department of Physics, University of California, Davis, CA, 95616, USA*

(Revised April 12, 2018)

ABSTRACT

We perform a kinematic and morphological analysis of 44 star-forming galaxies at $z \sim 2$ in the COSMOS legacy field using near-infrared spectroscopy from Keck/MOSFIRE and F160W imaging from CANDELS/3D-HST as part of the ZFIRE survey. Our sample consists of cluster and field galaxies from $2.0 < z < 2.5$ with K band multi-object slit spectroscopic measurements of their Hα emission lines. Hα rotational velocities and gas velocity dispersions are measured using the Heidelberg Emission Line Algorithm (HELA), which compares directly to simulated 3D data-cubes. Using a suite of simulated emission lines, we determine that HELA reliably recovers input $S_{0.5}$ and angular momentum at small offsets, but $V_{2.2}/\sigma_g$ values are offset and highly scattered. We examine the role of regular and irregular morphology in the stellar mass kinematic scaling relations, deriving the kinematic measurement $S_{0.5}$, and finding $\log(S_{0.5}) = (0.38 \pm 0.07)\log(M/M_\odot - 10) + (2.04 \pm 0.03)$ with no significant offset between morphological populations and similar levels of scatter (~ 0.16 dex). Additionally, we identify a correlation between $M_\star$and $V_{2.2}/\sigma_g$ for the total sample, showing an increasing level of rotation dominance with increasing $M_\star$, and a high level of scat-

Corresponding author: Leo Y. Alcorn
lyalcorn@tamu.edu

ter for both regular and irregular galaxies. We estimate the specific angular momenta (j_{disk}) of these galaxies and find a slope of 0.36 ± 0.12, shallower than predicted without mass-dependent disk growth, but this result is possibly due to measurement uncertainty at $M_\star < 9.5$. However, through a K-S test we find irregular galaxies to have marginally higher j_{disk} values than regular galaxies, and high scatter at low masses in both populations.

Keywords: galaxies – evolution, galaxies – kinematics and dynamics, galaxies – high-redshift, galaxies – clusters: general

1. INTRODUCTION

The ΛCDM model predicts galaxies build their angular momentum through tidal interactions until the dark matter halo virializes (White & Rees 1978; Fall & Efstathiou 1980; Mo et al. 1997). Dark matter-dominated gravitational potentials accrete primordial gas, which collapses into galaxy disks. The angular momentum of the baryonic disk of a galaxy has been shown to correlate with the angular momentum of the dark matter halo in the overall population of star-forming galaxies (SFGs), and is therefore a fundamental indicator of the total (baryonic and dark matter) growth of galaxies (Emsellem et al. 2007; Romanowsky & Fall 2012; Obreschkow & Glazebrook 2014; Cortese et al. 2016).

As the baryonic matter collapses to form a disk, angular momentum will be subject to change due to gas accretion or merging events (Vitvitska et al. 2002; Lagos et al. 2017; Penoyre et al. 2017). In the case of cold gas accretion, as matter accretes onto the gravitational potential, a torque on the galaxy can be exerted and the angular momentum increases with time (White 1984; Keres et al. 2004; Sales et al. 2012; Stewart et al. 2013; Danovich et al. 2015). In the case of minor or major mergers, the angular momentum can increase or decrease based on the geometry of the merger itself (Vitvitska et al. 2002; Puech et al. 2007; Naab et al. 2014; Rodriguez-Gomez et al. 2017). However in a number of cases, both observed and simulated, galaxies with clear signs of disrupted morphology show coherent rotation (Hung et al. 2015; Turner et al. 2017; Rodriguez-Gomez et al. 2017). This could be caused by a merger that is at the correct orientation to increase the angular momentum of the system. If major mergers are a significant part of galaxy evolution, then we should see a large scatter in angular momentum relations.

The mass - angular momentum plane can be mapped to the Fundamental Plane for spiral galaxies (Obreschkow & Glazebrook 2014), and the projection of this plane forms the Tully-Fisher Relation (TFR, Tully & Fisher 1977). However, high gas masses drive fundamental differences between local and high-redshift galaxies, most notably by increasing the star-formation rate (SFR), the increasing thickness of disks, the formation of large star-forming clumps, and the increased contribution of the gas velocity dispersion (σ_g) to the total kinematics of SFGs (Tacconi et al. 2010; Daddi et al. 2010; Obreschkow et al. 2016). The increase in σ_g could also be affected by cold-mode accretion or merging events, which could cause disk instabilities or loss of angular momentum (Hung et al. 2015). Kassin et al. (2007) accounted for the increased scatter of the TFR by including σ_g in the kinematic quantity $S_{0.5}$. The scatter of the $S_{0.5}$-$M_\star$ relation is smaller than the scatter of the stellar - mass TFR at all redshifts. $V_{2.2}/\sigma_g$ is also used in multi-object slit spectroscopic surveys to quantify the rotation support against random motions (Price et al. 2015; Si-

mons et al. 2017). However, significant scatter still remains in the TFR, $S_{0.5}$, and $V_{2.2}/\sigma_g$ spaces explored by recent high-redshift surveys. Median values of these datasets demonstrate the decrease of σ_g and increase of V_{rot} with time and stellar mass, possibly indicating kinematic downsizing and the formation of disky SFGs (Kassin et al. 2007; Simons et al. 2016, 2017).

In this work, we investigate the relationship between irregular morphology and kinematics. Due to the availablility high-resolution photometry by the Hubble Space Telescope (HST), we can examine the morphologies of galaxies at $z \sim 2$, in conjunction with the kinematic signatures provided by Keck/MOSFIRE (McLean et al. 2012). This will provide morphological signatures of recent merging events and irregular structure for our sample, which will allow us to determine if these morphologies are correlated with any kinematic effects such as increased σ_g, or an increased scatter in kinematic scaling relations in possible merging events.

These processes have been explored extensively and with great spatial precision in IFU surveys (Epinat et al. 2009a; Law et al. 2009; Förster-Schreiber et al. 2009; Swinbank et al. 2012; Wisnioski et al. 2015) (for a thorough review of these surveys, see Glazebrook 2013). However, since IFU data requires light from a source to be separated into different spaxels rather than integrated into a single slit, low-mass ($\log(M_\star/M_\odot) < 10.5$) and faint galaxies are not well-represented by these data (Wisnioski et al. 2015; Burkert et al. 2016). Additionally, these surveys also tend to exclude morphologically complex galaxies and galaxies with misaligned kinematic and morphological position angles (PA), as well as galaxies with $V_{2.2}/\sigma_g < 2$.

In contrast, surveys utilizing slit spectroscopy are more sensitive to low-mass and faint galaxies. Multi-object slit surveys demonstrate that the low-mass population is sensitive to the processes which affect angular momentum (Simons et al. 2016). These processes include star-formation feedback, disk instabilities caused by rapid accretion of surrounding gas, or mergers. This population is often more dispersion-supported and irregularly shaped than the higher mass population at $z \sim 2$. These low-mass objects can provide evidence for which processes shape galaxy evolution at the peak of cosmic star-formation history. In addition,slit surveys can measure larger data sets, over a variety of properties such as mass, luminosity, and environment. Here, we attempt to bridge the gap between IFU and slit surveys. To investigate the effects of slit against IFU spectroscopy, we simulate IFU data cubes, and project them through a slit to create a slit observation of an emission line.

Our data consist of objects from the COSMOS field (Capak et al. 2007) measured by the ZFIRE survey (Nanayakkara et al. 2016), including a $z = 2.095$ confirmed over-dense region in the COSMOS field (Spitler et al. 2011; Yuan et al. 2014). ZFIRE[1] targets galaxy clusters at $z \sim 2$ to explore galaxy evolution as a function of environment. ZFIRE combines deep multi-wavelength imaging with spectroscopy obtained from MOSFIRE to measure galaxy properties including sizes, stellar masses, star formation rates, gas-phase metallicities, and the interstellar medium (Kacprzak et al. 2015; Kewley et al. 2015; Tran et al. 2015; Kacprzak et al. 2016; Alcorn et al. 2016; Nanayakkara et al. 2016; Tran et al. 2016; Straatman et al. 2017; Nanayakkara et al. 2017).

In this work, we assume a flat ΛCDM cosmology with Ω_M=0.3, Ω_Λ =0.7, and H_0=70. At the cluster redshift, $z = 2.095$, one arcsecond corresponds to an angular scale of 8.33 kpc.

2. DATA

[1] zfire.swinburne.edu.au

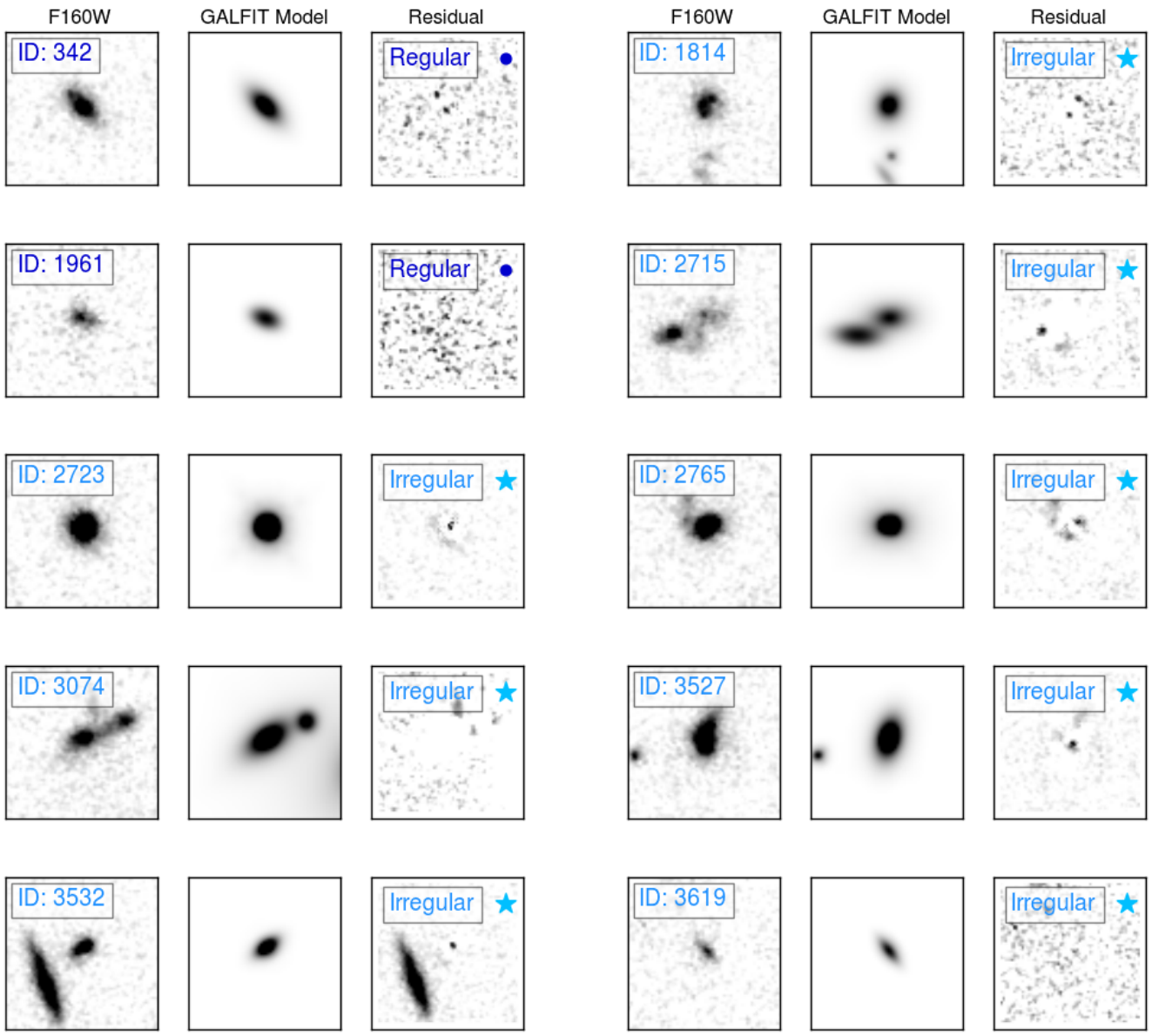

Figure 1. Imaging of our sample. Two galaxies are shown per row. From left for each galaxy: The F160W imaging from CANDELS/3D-HST. Center: Best-fit GALFIT model, and if the galaxy is considered "compact", it is noted. Right: Residual of the fit from the data. The residual is used to determine whether an object is regular or irregularly-shaped, and its classification is noted in this panel. Regular galaxies are in dark blue, and are plotted as dark blue circles in the text. Irregular galaxies are in light blue, and are plotted as light blue stars in the text. Compact galaxies of either classification are unfilled circles or stars.

2.1. *Sample Selection*

Our sample is drawn from the ZFIRE survey (Nanayakkara et al. 2016), a spectroscopic follow-up of ZFOURGE photometry (Straatman et al. 2016). To summarize, we identify star-forming galaxies (SFGs) within a photometric redshift range of $1.7 < z < 2.5$ in ZFOURGE NIR imaging of COSMOS fields. ZFOURGE combines broad-band imaging in K_s and the medium-band J_1, J_2, J_3, H_s, and H_l filters to select objects using K_s-band images with a 5σ limit of 25.3 AB magnitudes. Rest-frame UVJ colors are used to identify SFGs, which will have prominent emission lines. Objects with radio, infrared, ultraviolet, or x−ray indications of AGN activity (identified via Cowley et al. 2016) are rejected from this analysis.

The COSMOS protocluster was initially identified in Spitler et al. (2011) using photometric redshifts from ZFOURGE and subsequently confirmed with spectroscopic redshifts from MOSFIRE (Yuan et al. 2014). This overdensity consists of four merging groups, and is projected to evolve into a Virgo-like cluster at $z = 0$. Cluster members are identified to redshifts within $2.08 < z < 2.12$.

ZFOURGE uses FAST (Kriek et al. 2009) to fit Bruzual & Charlot (2003) stellar population synthesis models to the galaxy spectral energy distributions to estimate observed galaxy properties. After spectroscopic redshifts were obtained on MOSFIRE, objects were run in FAST using the spectroscopically confirmed redshifts rather than the photometric redshifts, providing our stellar masses and attenuation values (A_V). We assume a Chabrier (2003) initial mass function with constant solar metallicity and an exponentially declining star formation rate, and a Calzetti et al. (1999) dust law.

2.2. *HST Imaging*

Our morphological measurements are from the Cosmic Assembly Near-Infrared Deep Extragalactic Survey (Grogin et al. 2011; Koekemoer et al. 2011, CANDELS) imaging processed by the 3D-HST team (v4.1 data release) Skelton et al. (2014). Our PSF is also constructed by the 3D-HST team. We use GALFIT software (Peng et al. 2010) to measure galaxy sizes from the F160W imaging. At $z \sim 2$, F160W corresponds to rest-frame g-band. Our morphological fitting is summarized in Alcorn et al. (2016) but we briefly repeat here.

We generate a custom pipeline to fit the 161 COSMOS galaxies in ZFIRE with F160W imaging using initial measurements of size, axis ratio (q), position angle (PA), and magnitude from SExtractor. Objects within $2''$ of a target galaxy are simultaneously fit with the central object. Residual images are visually inspected to determine the best possible fits for each galaxy. Galaxies with poor residuals are re-fit using a modified set of initial parameters. Galaxies were restricted to Sérsic indices (n) between 0.2−8.0. If objects iterated to the boundaries of our Sérsic constraints, they were refit with a fixed Sérsic index ($n = 1.0$ for objects which went to $n = 0.2$, and $n = 4.0$ for objects which went to $n = 8.0$) Our results are consistent within 2σ to van der Wel et al. (2014) (see Table 1).

25 objects in our final sample are considered to be regular galaxies by evaluation of GALFIT residuals. Examples of our sample showing regular and irregular galaxies by our criteria are shown in Figure 1. To determine the presence of irregular morphology or tidal features, we examine residual images. Using segmentation maps from SExtractor, we isolate the individual galaxies and measure the residual, the sky flux, and the flux of the original object. If residual levels are at more than 2 times the level of the sky, and more than 25% of the flux of the original object remains, we determine the presence of significant artifacts. If residual images show significant artifacts, which indicate

Table 1. Morphological measurements from F160W imaging.

ID	Cluster/Field	Regular/Irregular	R_e (arcseconds)	Sersic Index	Axis Ratio	PA
1814	Field	Irregular	0.29±0.01	1.0±0.0	0.8±0.0	-11.6±3.7
1961	Field	Regular	0.28±0.01	0.4±0.1	0.6±0.0	68.6±2.3
2715	Cluster	Irregular	0.46±0.01	0.9±0.1	0.6±0.0	-87.4±1.3
2723	Cluster	Irregular	0.13±0.11	2.6±5.4	0.9±0.9	20.7±32.7
2765	Field	Irregular	0.34±0.01	4.0±0.0	0.7±0.0	-87.8±2.0
3074	Field	Irregular	0.46±0.01	1.0±0.0	0.5±0.0	-55.7±0.8
342	Field	Regular	0.38±0.01	0.8±0.0	0.5±0.0	44.7±0.6
3527	Field	Irregular	0.38±0.01	0.9±0.0	0.5±0.0	-12.8±0.5
3532	Cluster	Irregular	0.20±0.01	0.9±0.1	0.4±0.0	-54.4±0.9
3619	Field	Irregular	0.25±0.01	0.7±0.2	0.2±0.0	37.1±1.3
3633	Cluster	Regular	0.59±0.01	0.8±0.1	0.3±0.0	-85.1±0.6
3655	Field	Irregular	0.54±0.01	0.7±0.0	0.9±0.0	44.5±2.6
3680	Field	Irregular	0.34±0.01	0.6±0.1	0.5±0.0	-11.6±1.6
3714	Field	Irregular	0.32±0.01	0.9±0.0	0.7±0.0	1.3±0.2
3842	Cluster	Irregular	0.43±0.01	0.9±0.0	0.5±0.0	-54.9±0.6
3844	Field	Irregular	0.66±0.02	1.0±0.0	0.7±0.0	-60.8±1.8
3883	Field	Regular	0.19±0.01	0.9±0.2	0.8±0.1	29.3±9.3
4010	Field	Regular	0.29±0.01	0.6±0.1	0.6±0.0	-8.7±1.0
4037	Field	Regular	0.38±0.01	0.6±0.0	0.7±0.0	-52.9±1.7
4091	Cluster	Regular	0.33±0.01	0.3±0.1	0.5±0.0	-88.5±0.5
4099	Field	Irregular	0.38±0.01	1.2±0.1	0.8±0.0	-11.1±3.8
4267	Field	Regular	0.30±0.01	1.0±0.0	0.3±0.0	29.4±1.3
4461	Field	Regular	0.30±0.01	4.0±0.0	0.9±0.1	-83.6±1.5
4488	Field	Regular	0.35±0.01	0.6±0.1	0.5±0.0	-71.3±1.2
4645	Cluster	Regular	0.33±0.01	0.4±0.1	0.3±0.0	-0.6±0.9
4724	Field	Regular	0.68±0.22	8.0±2.0	0.3±0.0	-82.4±1.5
4746	Field	Regular	0.14±0.01	0.9±0.1	0.5±0.0	-59.2±2.7
4796	Field	Regular	0.29±0.01	0.8±0.1	0.4±0.0	85.8±1.7
4930	Cluster	Irregular	0.39±0.01	1.0±0.0	0.1±0.0	88.6±0.5
5269	Cluster	Regular	0.54±0.01	0.5±0.0	0.5±0.0	-15.9±0.8
5342	Field	Regular	0.14±0.01	1.0±0.2	0.4±0.0	10.3±2.3
5408	Cluster	Regular	0.24±0.01	1.0±0.1	0.6±0.0	-76.9±2.1
5630	Field	Regular	0.38±0.01	1.4±0.1	0.3±0.0	-34.8±0.5
5745	Cluster	Regular	0.10±0.01	2.7±0.6	0.8±0.1	-37.1±12.1
5870	Cluster	Regular	0.38±0.01	0.7±0.0	0.7±0.0	-75.8±2.1
6485	Field	Regular	0.33±0.01	1.1±0.1	0.6±0.0	89.5±0.5
6908	Field	Irregular	0.51±0.01	0.5±0.0	0.9±0.0	-15.2±2.1
6954	Field	Regular	0.24±0.01	0.6±0.1	0.3±0.0	-34.9±1.0
7137	Field	Regular	0.36±0.01	1.1±0.1	0.7±0.0	-83.6±1.7
7676	Field	Irregular	0.54±0.01	0.7±0.1	0.2±0.0	26.4±0.5
7774	Field	Regular	0.24±0.01	1.2±0.2	0.8±0.1	-52.1±10.4
7930	Cluster	Irregular	0.53±0.03	2.5±0.2	0.2±0.0	13.1±0.5
8108	Field	Irregular	0.29±0.01	1.0±0.0	0.4±0.0	-34.8±1.2
9571	Cluster	Regular	0.48±0.03	4.0±0.0	0.6±0.0	11.0±2.9

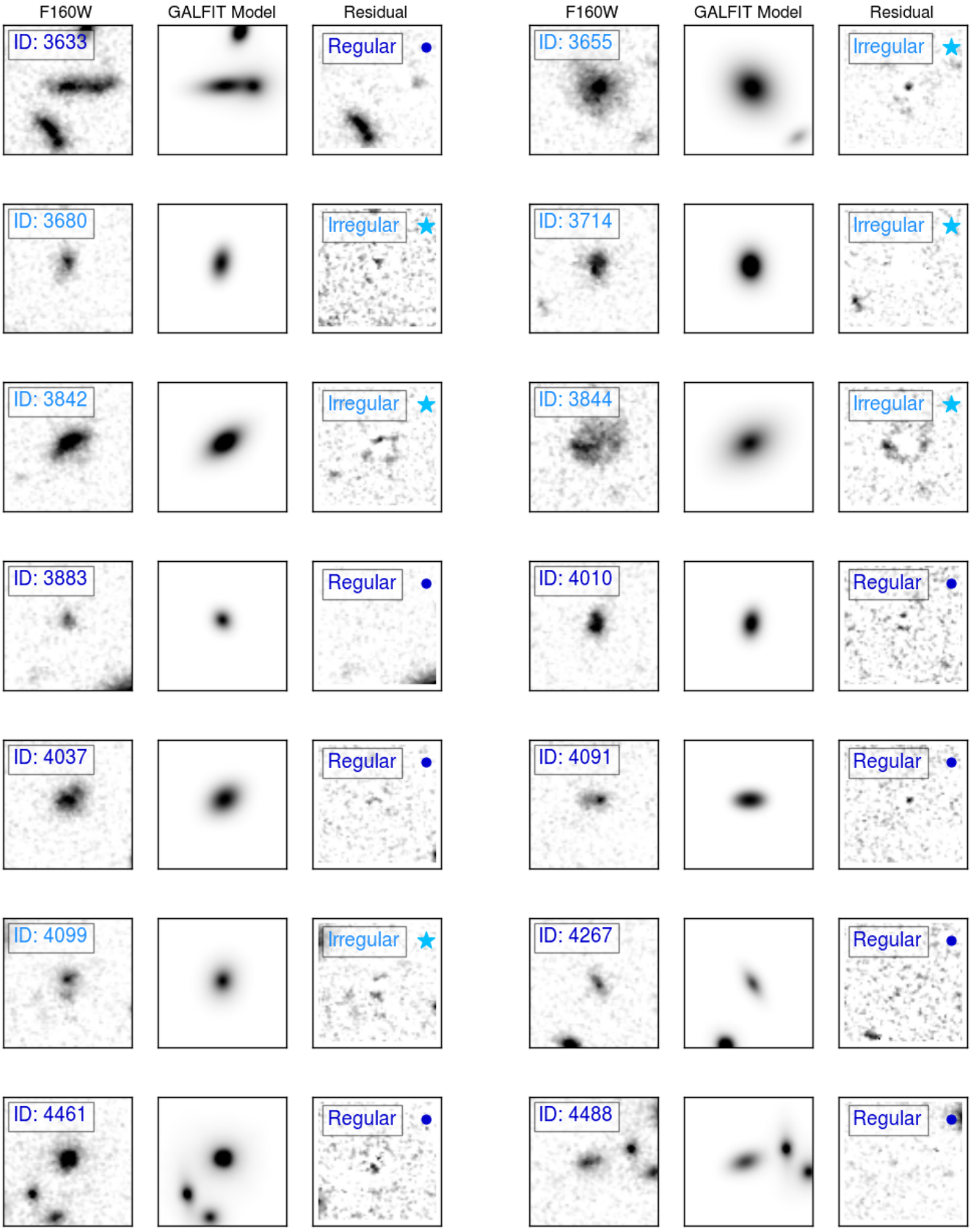

Figure 1. Continued

that a Sérsic profile is a poor or unreliable fit to the object, they are flagged as irregulars, although this population could include both irregulars and merging objects. Conversely, regulars show no significant residuals (residual levels are less than 2 times sky levels and less than 25% the flux levels of the object) when fit with a Sérsic profile. These values were determined empirically, although small changes do not significantly change our results.

In both cases, the presence of close companions was neglected in the absence of strong residuals, as we cannot spectroscopically confirm the redshifts of nearby objects. This method is possibly biased toward classifying smaller galaxies ($< 0.3''$) as regular galaxies, because residual values are only measured in areas identified as being associated with the original object. Additionally, objects that are photometrically irregular may be kinematically regular, such as clumpy disks, and may not be distinct from regular galaxies apart from their photometry. When comparing our populations through a two-population KS test, we find a similar distribution of stellar masses from $9.0 \leq \log(M_\star) \leq 11.0$ and Sérsic index from $0.2 < n < 8.0$. See Figure 2.

We include a category of "compactness" in our final sample, where objects with an effective radius r_e smaller than the HST F160W PSF FWHM ($r_e < 0.19''$, or 1.58 kpc at $z = 2.095$) (Skelton et al. 2014) are compact. These objects are marked as unfilled points in our figures and are morphologically unresolved. From van der Wel et al. (2014) the median size of late-type galaxies at $z \sim 2$ in our M_* range is 2-4 kpc, thus we are confident that our adopted compactness threshold of 1.58 kpc is appropriate. This is in contrast to objects that are kinematically unresolved, where their diameter is less than the seeing limit (See Table 2). 21 galaxies in this sample are kinematically unresolved. The velocity of these unresolved sources is often underestimated (Newman et al. 2012), but we include compact objects with reliable velocity measurements (Section 3.1).

2.3. *MOSFIRE NIR Spectroscopy*

Observations were taken in December 2013 and February 2014 in the K-band filter covering 1.93-2.45 μm, the wavelength range we would expect to see Hα and [N II] at the cluster redshift. Seeing varied from $\sim 0.4''$ to $\sim 1.3''$ over the course of our observations.

The spectra are flat-fielded, wavelength calibrated, and sky subtracted using the MOSFIRE data reduction pipeline (DRP)[2]. A custom ZFIRE pipeline corrected for telluric absorption and performed a spectrophotometric flux calibration using a type A0V standard star. We flux calibrate our objects to the continuum of the standard star, and use ZFOURGE photometry as an anchor to correct offsets between photometric and spectroscopic magnitudes. The final result of the DRP are flux-calibrated 2D spectra and 2D 1σ images used for error analysis. For more information on ZFIRE spectroscopic data reduction and spectrophotometric calibrations, see Nanayakkara et al. (2016). 1D spectra and catalogs are available to the public on the ZFIRE website.

From spectroscopic observations, we reject objects with only one identified emission line, without morphological measurements, or with AGN signatures (Cowley et al. 2016), leaving 92 SFGs with K band spectroscopy.

2.4. *PSF Fitting*

The assumed PSF for an observation plays a role in the recovery of accurate velocities, as the mischaracterization of the shape of the PSF can result in an underestimation of the velocity. In most cases, a Gaussian PSF with a FWHM given by seeing conditions is convolved with the emission-line fit, but in recent work it

[2] http://keck-datareductionpipelines.github.io/MosfireDRP/

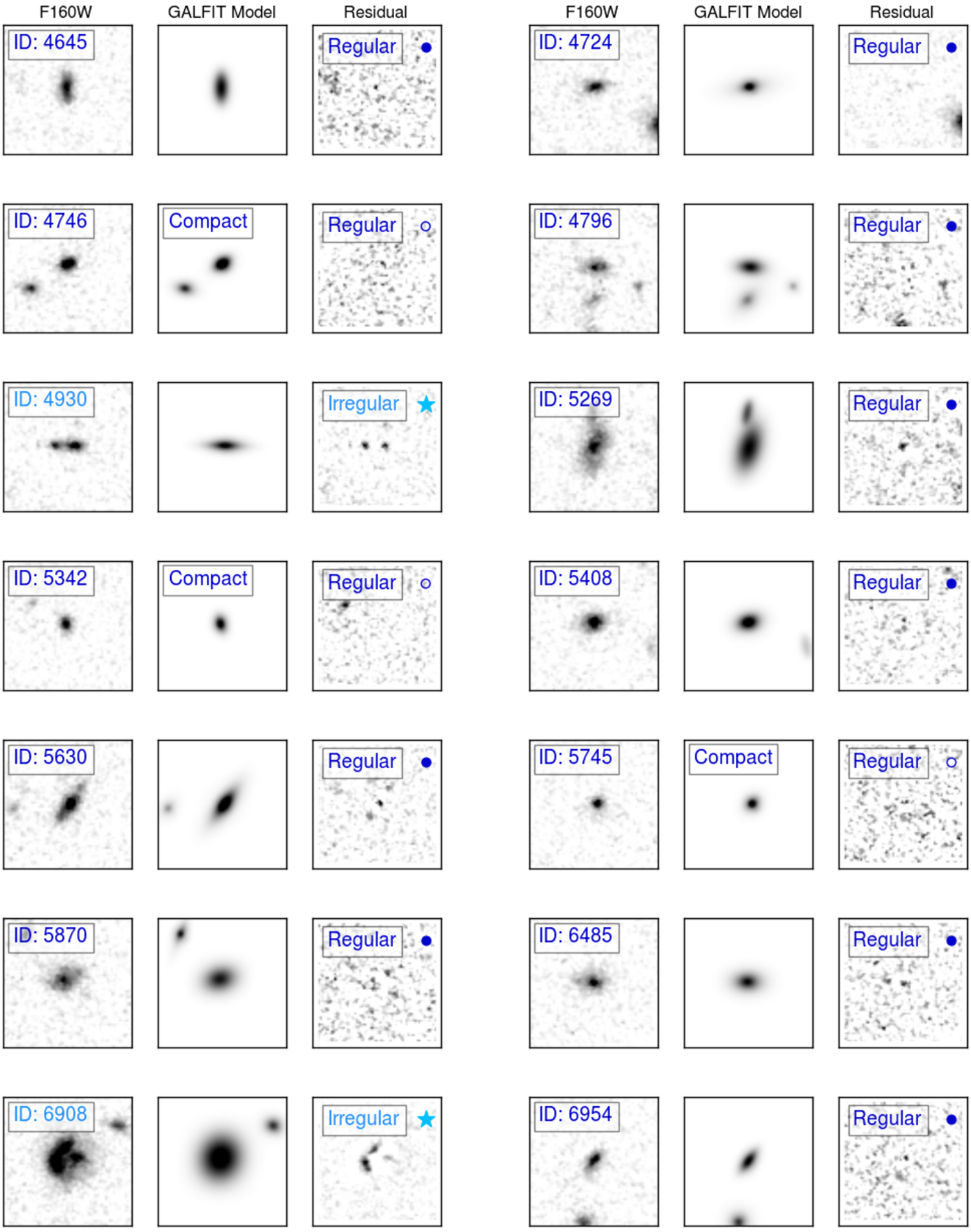

Figure 1. Continued

has been shown that on the MOSFIRE instrument, a Moffat profile is a better fit to the PSF (Straatman et al. 2017). Therefore we fit and apply Moffat PSFs to all objects in our sample.

To determine our PSF, we create a 2D Moffat-profile simulated star. We collapse this star into a flat spectral profile and sum along the wavelength component to estimate the spatial 1D profile of the star, and subtract the profile on either side of the peak at the positions of our dithering pattern (1.25″) to correctly account for any effect of the dither pattern on the wings of the PSF. Then for each observed mask, we sum along the wavelength plane to determine the spatial profile of our flux monitor star. We leave the Moffat parameters α and β free and fit the Moffat profile given as

$$PSF(r) = \frac{\beta - 1}{\pi \alpha^2} \left[1 + \left(\frac{r}{\alpha}\right)^2\right]^{-\beta}, \qquad (1)$$

to our observed flux monitor stars, and use the best-fit values for the Moffat parameters to apply to our Moffat convolution kernel when we fit our emission lines. If the wings of the best-fit Moffat profile appear to over-fit the observed star, we fix $\beta = 2.5$ and refit to find α. The best fit Moffat parameters used to generate our emission line models can be seen in Table 2.

3. METHODS

3.1. *Spectroscopic Fitting Method*

Our fitting procedure for our sample and our simulated observations are based around HELA (Heidelberg Emission-Line Algorithm), which was developed by C.M. Straatman (Straatman in prep). Information on the models generated by HELA is located in the Appendix.

We emphasize that there are many ways to refer to the velocity of a galaxy. In this text, we refer to velocity in three main ways. $V_{rot}(r)$ is the rotational velocity at a given radius of a galaxy, referred to as simply the rotational velocity in this text. This is in contrast to V_t, which is the asymptotic velocity (at the flat part of the rotation curve). Additionally we use $V_{2.2}$, which is the velocity at $2.2r_s$, where the rotation curve of an ideal disk peaks (Freeman 1970), and is used widely in literature as a common reference point for velocity (Miller et al. 2011).

To determine best-fit parameters for our emission line, our procedure is thus:

1. Identify the position of the Hα emission line. Subtract continuum values if present (see Section 3.3).

2. Mask wavelengths which are strongly contaminated by sky emission in the observed spectra, or which are bad pixels.

3. Determine fitting bounds: -600 km s^{-1}< V_t < 600 km s^{-1}, 10 km s^{-1}< σ_g < 150 km s^{-1}, 0.1″ < r_s < 1″, and 0.03″ < r_t < r_s (we also perform fitting where r_t is fixed to $r_t = 0.33r_s$ or $r_t = 0.4r_s$). Position of the intensity peak cannot shift more than three pixels from given coordinates. These values and the intensity are all free parameters.

4. Run the simulated emission line through HELA (see Appendix) to derive best-fit parameters. We use a Markov-Chain Monte-Carlo analysis (MCMC) initializing 30 walkers over 1000 steps. Our walkers are initialized as a clump, values randomly distributed around the given wavelength and spatial position, and initial guess for V_t, σ_g, $r_s = r_e/1.678$ (where r_e is the effective radius measured from GALFIT), and $r_t = 0.3r_s$, or r_t fixed. We use the Python package emcee for our MCMC algorithm[3] (Foreman-Mackey et al. 2012).

5. Discard the first 200 iterations out of a total of 1000 - where the MCMC algo-

[3] http://dan.iel.fm/emcee/current/

Table 2. Mask properties and best-fit Moffat parameters.

Date	Mask	Average Seeing ($''$)	α	β	Slit PA (^{o})[a]
Dec 2013	Shallowmask1	0.7	0.601	2.487	134
Dec 2013	Shallowmask2	0.68	0.581	2.5	-47.3
Dec 2013	Shallowmask3	0.7	0.674	2.778	14.8
Dec 2013	Shallowmask4	0.67	0.516	2.574	-63
Feb 2014	DeepKband1	1.27	1.031	2.5	2
Feb 2014	DeepKband2	0.7	0.656	2.599	-62
Feb 2014	KbandLargeArea3	1.1	1.021	2.5	59
Feb 2014	KbandLargeArea4	0.66	0.489	2.525	2

[a] PA is defined as east of north.

rithm tends to be far from convergence. Our best-fit model is taken to be the median of the posterior likelihood output of all our free parameters after convergence, and errors are the 16th and 84th percentiles of the walkers. The value for $V_{2.2}$ is determined by fitting the velocity curve function (Equation B11) to each walker and step, and then measuring the median value.

6. In the case of multiple peaks in the posterior likelihood, we isolate one peak and fit a Gaussian to the largest peak to determine the best-fit values. Errors on the fit are determined from the σ value on this Gaussian fit.

We reject four compact galaxies with errors greater than $0.8V_{2.2}$ where $V_{2.2}>$ 35 km s^{-1}, which are considered unreliable. Six morphologically resolved galaxies with similar kinematics were kept in the sample and are shown as upper limits on the TFR (Figure 3).

3.2. *Fitting ZFIRE Data*

Our fitting algorithm is applied to the 2D telluric and spectrophotometrically corrected emission lines. Faint continua are seen in a small number of objects, so we subtract a flat continuum when one is detected. Continuum subtraction is performed in the same method as Straatman et al. (2017). Summarized, for each row of pixels in a stamp 300 $\AA$ wide, we determine a median flux with outlier pixels $> 2.5\sigma$ above the median rejected, and any sky or Hα [N II] emission masked. This procedure is repeated a total of three times, then the median values are subtracted from each row.

The measured axis ratio from GALFIT is used to determine the inclination for use in our fitting procedure:

$$\sin i = \sqrt{\frac{1-q^2}{1-q_0^2}}, \tag{2}$$

where $q_0 = 0.19$ (Miller et al. 2011). 40 objects with galaxy PA-slit offset $\Delta\alpha > 45^o$ or $\Delta\alpha < -45^o$, where PA is determined from GALFIT modeling, are rejected from the final sample, although objects with large PA uncertainties (mostly objects with low inclination or high q) that could overlap within this range are not rejected. We also reject objects with significant sky emission (3 objects where more than 50% of the line is masked, Appendix B.1) or where SNR < 5 (5 objects).

4. RESULTS

Our final sample consists of 44 galaxies within $-45^o < \Delta\alpha < 45^o$ and with less than half the emission line masked and SNR > 5. 14 of these objects are associated with an over-density at $z = 2.095$, and 30 are field objects. Due to the small number of cluster objects in our sample, as well as the lack of 1D environmental distinc-

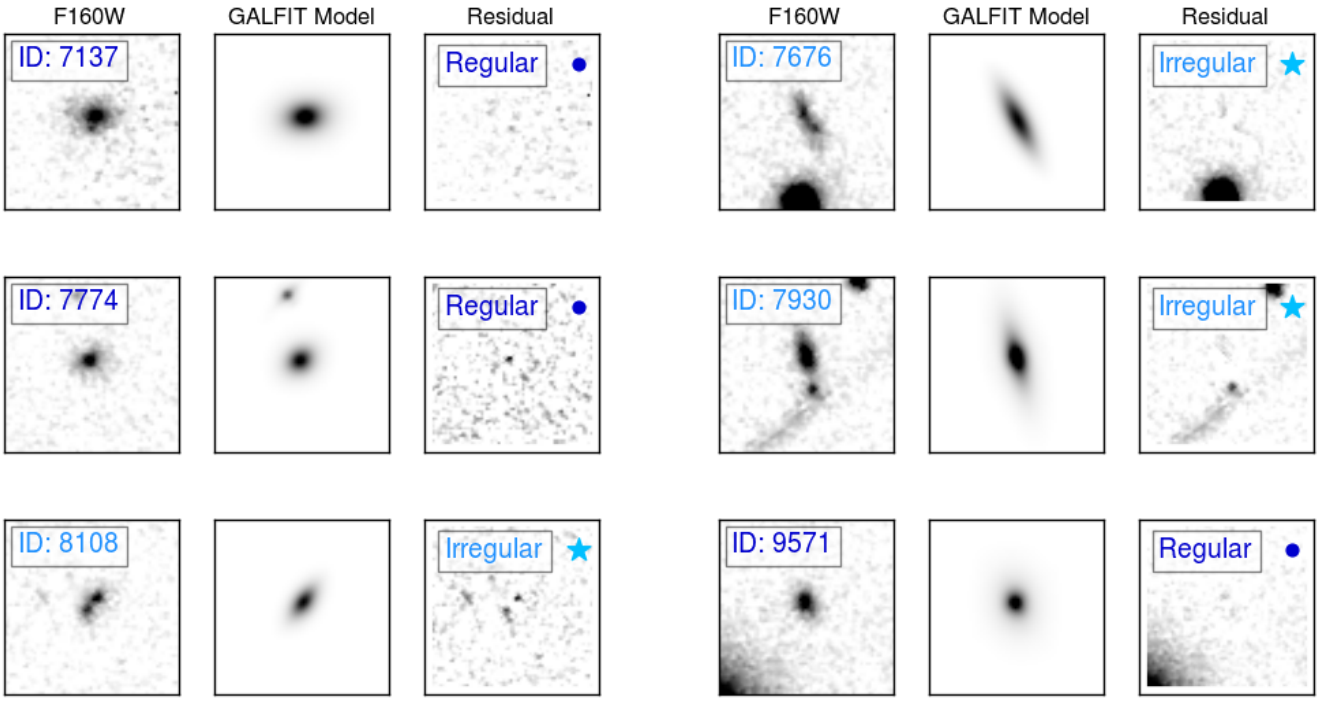

Figure 1. Continued

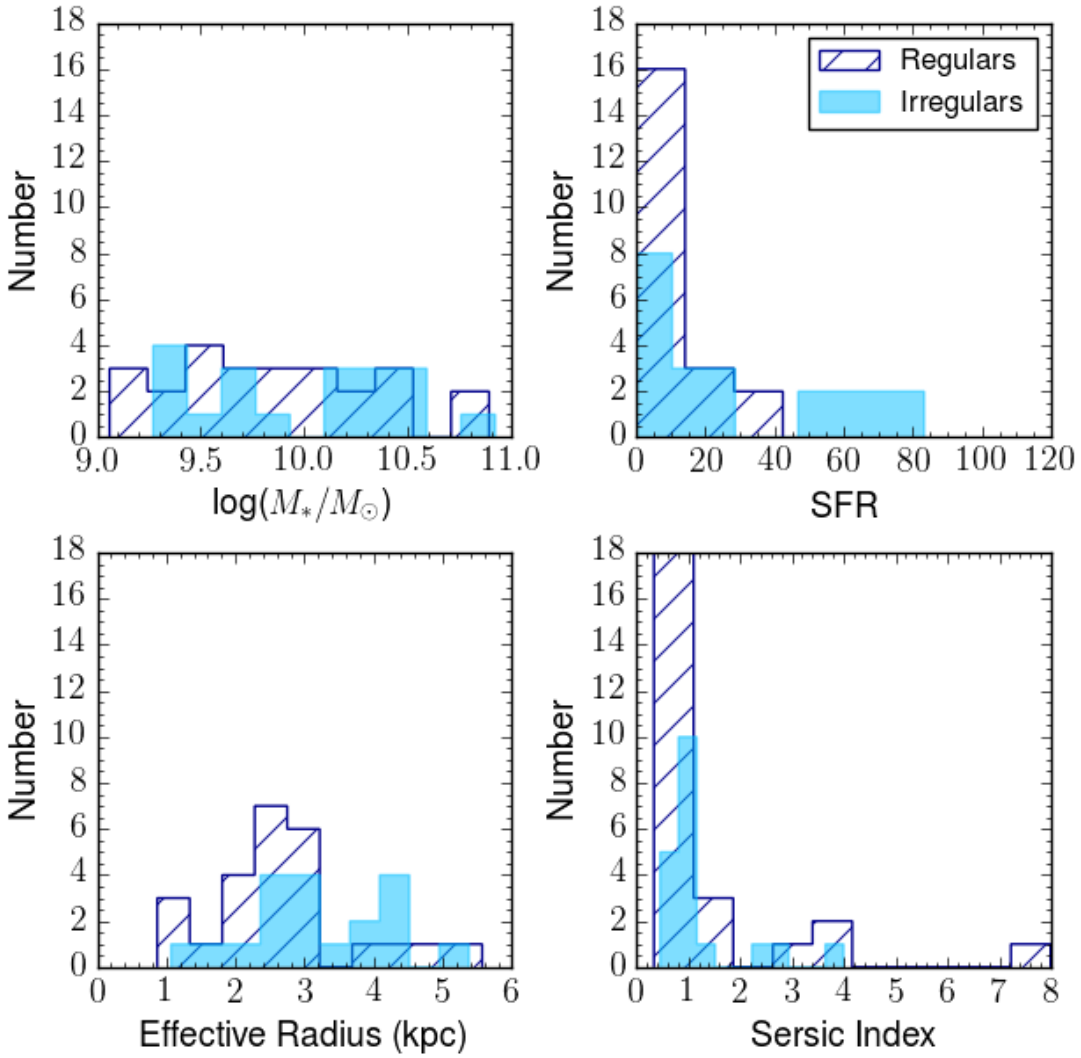

Figure 2. Histograms of our galaxy populations. Light blue solid bins are irregular galaxies, and dark blue hatched bins are regular galaxies. By applying a two-population KS test, we find similar properties in both populations, although irregulars are marginally more likely to have higher star-formation rates.

tions in this sample (Alcorn et al. 2016), we do not include any environmental analysis in this work. We identify 25 regular-type galaxies in our sample, and 19 galaxies which could include both merging galaxies and irregular galaxies - anything that is not well-described by a Sérsic profile. Wisnioski et al. (2015) determines a disk fraction of 58% at $z \sim 2$, similar to our estimated disk (regular) fraction (56.8%) determined from measuring the residual values after subtracting a Sérsic fit.

4.1. *Measured Kinematic Scaling Relations*

We derive a best fit linear relation using the Levenberg - Marquardt algorithm for the TFR of the form

$$\log(V_{2.2}) = A \log(M_*/M_\odot - 10) + B, \qquad (3)$$

weighted by the errors on $V_{2.2}$ (Figure 3, left). We reject objects greater than 3σ from the fit, and iterate the fit until the process converges. Ranges on the fitting parameters are determined by bootstrapping the sample 1000 times. In the case where A and B are both free parameters of the linear fit, we derive $A = 0.29 \pm 0.1$ and $B = 2.19 \pm 0.04$ for the total sample. The

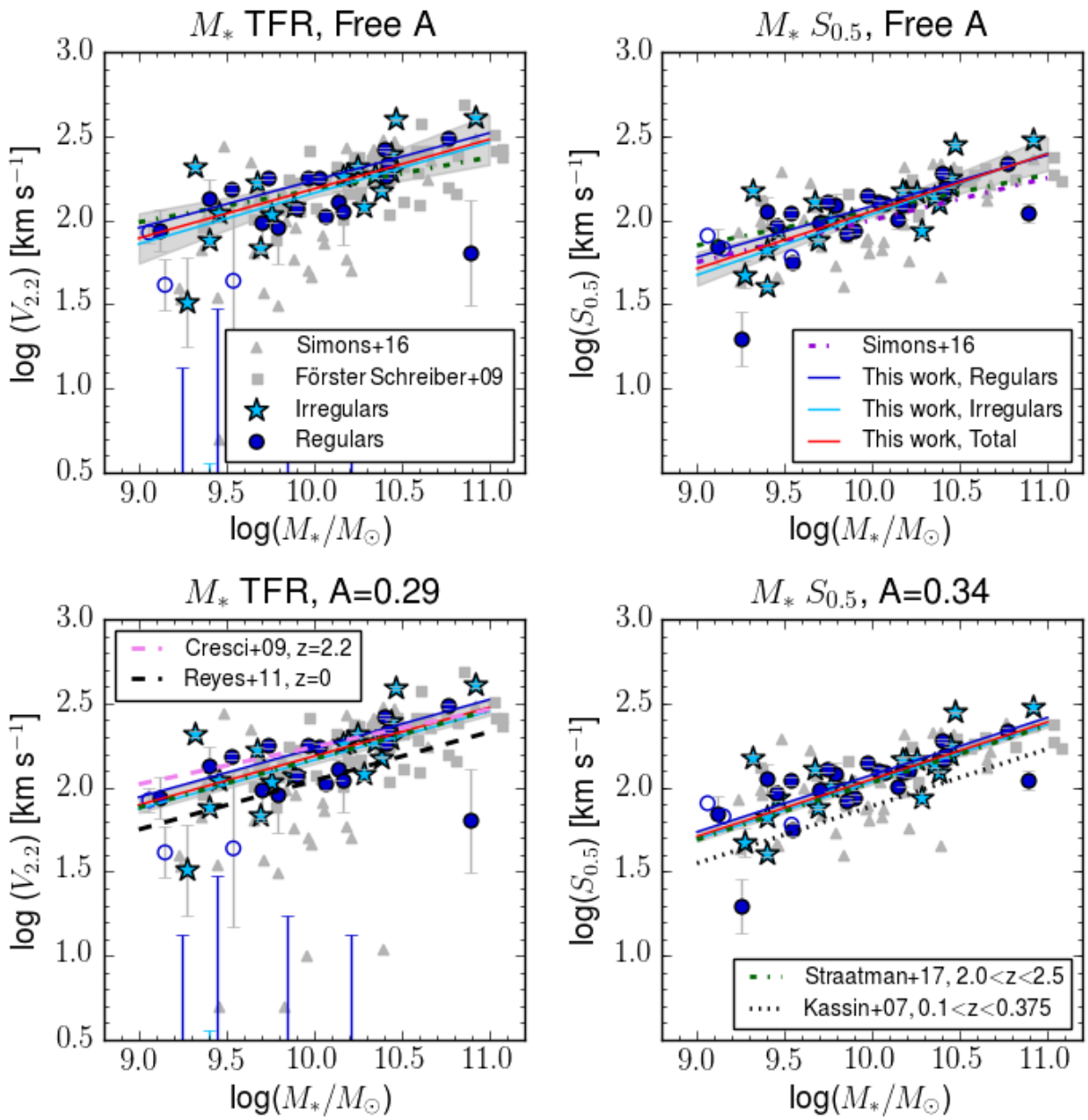

Figure 3. Kinematic scaling relations of the ZFIRE sample. Irregular galaxies are light blue stars, and the linear fit to irregular galaxies is the light blue line. Regular galaxies are dark blue circles, and the fit is the dark blue line. Compact galaxies of either population are unfilled circles or stars. Galaxies with unreliable velocity measurements are shown as upper limits. The best-fit linear relation to the total sample is the solid red line, and the grey shaded regions show the uncertainty in the best-fit line. The best-fit lines from Straatman et al. (2017) are the green dashed line. Upper Left: The stellar-mass TFR. We compare to the SIGMA sample (grey triangles) (Simons et al. 2016) and the SINS data points (grey squares) (Förster-Schreiber et al. 2009). Lower Left: As upper left, with slope fixed to $A = 0.29$ for consistency with the $z = 0$ TFR (black dashed) (Reyes et al. 2011) and the SINS IFU survey (pink dashed) (Cresci et al. 2009). Upper Right: The stellar-mass $S_{0.5}$ relation from Kassin et al. (2007), which includes the contribution of σ_g to the total kinematics of the system, and a comparison to Simons et al. (2016). Lower Right: Slope is fixed to $A = 0.34$. We compare to their relation at $0.1 < z < 1.2$ and find an offset of 0.16±0.04 dex higher $S_{0.5}$ at a given stellar mass.

irregular and regular populations are offset by 0.08 dex. Scatter in all populations is high, at 0.5 ± 0.02 dex for the total sample, 0.6 ± 0.02 for regulars, and 0.39 ± 0.03 for irregulars. Given this high level of scatter, we do not think our offsets are significant. There are a number of low-mass objects that are significantly offset from the relation - these are the compact galaxies that could have underestimated velocities (Newman et al. 2012).

To compare our values for the TFR to literature values, in particular to determine a possible offset to local relations and IFU observations, we hold $A = 0.29$, determined by Reyes et al. (2011) for the local TFR. We derive an offset of $\Delta M/M_{\odot}$=-0.34±0.22 from local relations.

In both free and fixed slope cases, we do not find any statistically significant difference between irregulars and regulars. Our results for the TFR do not change if we remove compact objects from our fitting.

In addition, given the values of both $V_{2.2}$ and σ_g, we derive a best-fit relation for $S_{0.5}$, defined in Kassin et al. (2007) as $S_{0.5} = \sqrt{0.5V_{2.2}^2 + \sigma_g^2}$. This equation is derived from a combined velocity scale S_K (Weiner et al. 2006), $S_K^2 = KV_{rot}^2 + \sigma^2$, where K is a constant $\leqslant 1$. Where rotation curves have been measured, $K = 0.3 - 0.5$, consistent with the prediction for an isothermal potential and a flat rotation curve. This suggests that S_K is a good tracer for the gravitational potential, and for consistency with the literature we use $K = 0.5$.

When we derive our equation of the form $\log(S_{0.5}) = A\log(M/M_{\odot} - 10) + B$ to the data, we find best fit parameters of 0.38 ± 0.07 and 2.04 ± 0.03 (Figure 3, Right). When we fix $A = 0.34$ (seen in $0.1 < z < 1.2$ from Kassin et al. (2007)) we measure $B = 2.05 \pm 0.03$. Scatter in all populations decreases significantly when we include the contribution of σ_g to the total kinematics (from 0.5 dex for the TFR to 0.15 dex for $S_{0.5}$). Kassin et al. (2007) derives a scatter of 0.16 dex in $S_{0.5}$ for $0.1 < z < 1.2$, similar to Price et al. (2015) who find a scatter of 0.17 dex at $1.4 < z < 2.6$. Straatman et al. (2017) finds consistent values with these at $2.0 < z < 2.5$ (0.15 dex), using 22 galaxies drawn from the same ZFIRE sample as this paper, 20 of which are in common with our sample. Our offset implies a zero-point evolution of $\Delta M/M_{\odot}$=-0.47±0.14.

When we hold $r_t = 1/3r_s$ and $r_t = 0.4r_s$, we find our results for both the $M_{\star}$-TFR and $S_{0.5}$ do not significantly change. Our simulated MOSFIRE observations (Appendix B), show that we tend to overestimate our values for $S_{0.5}$ to a median offset of ∼10% (Figure 12, top two rows). However, this offset is stable for SNR>10 and less than half the emission line masked (see Appendix B.1), indicating our $S_{0.5}$ values are reliable.

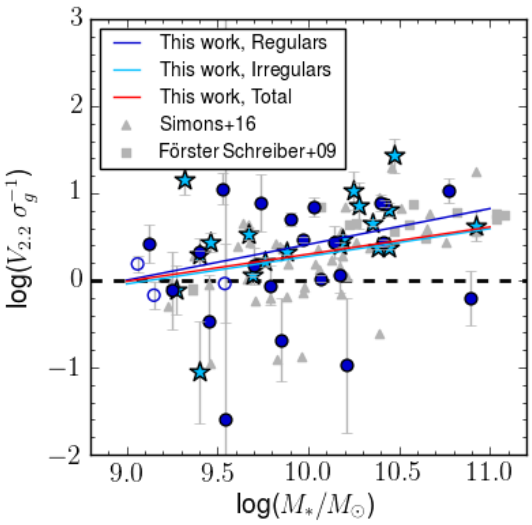

Figure 4. $V_{2.2}/\sigma_g$ of galaxies in the ZFIRE sample, showing the ratio of rotational support (measured at $V_{2.2}$) and σ_g, pressure support. We find consistent values between regulars and irregulars, and a clear relation between the rotational support and stellar mass. Colors and markers are as described in Figure 3. The black dashed line shows equal rotation and pressure support.

The $V_{2.2}/\sigma_g$ parameter derived from $V_{2.2}$ and σ_g is an instructive measurement for determin-

ing the amount of rotational dominance in integrated kinematics. Higher $V_{2.2}/\sigma_g$ indicates a well-ordered rotating disk with minimal random motion within the disk, whereas lower $V_{2.2}/\sigma_g$ signals a stronger presences of random motion. In Förster-Schreiber et al. (2009); Wisnioski et al. (2015); Turner et al. (2017) galaxies are considered rotation-dominated at $V_{2.2}/\sigma_g > 1$ and pressure-dominated at $V_{2.2}/\sigma_g < 1$. Within our sample we observe both pressure-dominated and rotation-dominated galaxies.

We see a highly scattered trend between $M_\star$ and $V_{2.2}/\sigma_g$, where objects with smaller $M_\star$ are more likely to have $\log(V_{2.2}/\sigma_g) < 0$ (Figure 4). We can see a clear trend in all populations of increasing rotation support at increasing stellar mass. In Figure 8 we can see this is not due to a decrease in pressure support at high mass, as σ_g values are unrelated to the stellar mass of a galaxy. Scatter is large for all populations, 0.67 ± 0.04 dex for irregulars and 0.53 ± 0.01 dex for regulars. The median values of $V_{2.2}/\sigma_g$ for regular and irregular galaxies were 1.55 and 2.75, respectively, but given high levels of scatter in both populations, it is unclear if this difference is significant. The median value of $V_{2.2}/\sigma_g$ for the total sample was 2.48. Again, our results are not significantly affected by holding r_t to a fixed position relative to r_s.

Our MOSFIRE simulations (Appendix B) show difficulty in recovering $V_{2.2}/\sigma_g$ using slit spectroscopy. In the bottom two panels of Figure 12, we see that we tend to overestimate $V_{2.2}/\sigma_g$ values by 25% of the input, with scatter of around 20%. This leads us to believe our values could be unreliable and could be related to the heavy scatter in our measured values for $V_{2.2}/\sigma_g$.

Table 3. Kinematic measurements of ZFIRE galaxies using HELA

ID	Date	Mask	z_{spec}	M_*	SFR[a]	$V_{2.2}$	σ_g	j_{disk}
1814	feb2014	KbandLargeArea4	2.17	9.76	14.6	108.44±13.19	66.19±3.55	321.87±39.63
1961	feb2014	KbandLargeArea3	2.31	9.79	N/A	90.85±46.57	103.72±8.78	241.22±123.8
2715	dec2013	mask2	2.08	9.88	13.7	119.38±5.98	55.18±4.51	555.5±30.6
2723	dec2013	mask2	2.09	10.92	N/A	406.46±16.23	96.47±37.72	717.42±616.43
2765	dec2013	mask1	2.23	10.44	83.3	193.38±4.42	80.17±2.42	1227.22±46.26
3074	dec2013	mask1	2.23	10.19	N/A	186.93±9.12	63.69±9.9	879.78±45.46
342	feb2014	KbandLargeArea4	2.15	10.42	31.3	218.5±3.04	28.66±2.65	823.63±15.56
3527	feb2014	KbandLargeArea4	2.19	10.38	56.1	151.4±1.39	64.26±1.65	579.59±7.11
3532	dec2013	mask1	2.1	9.4	9.9	3.57±4.8	40.39±1.31	7.27±9.77
3619	feb2014	KbandLargeArea3	2.29	9.27	3.3	32.43±20.07	41.56±6.78	81.71±50.66
3633	dec2013	mask1	2.1	10.4	42.4	315.97±8.34	33.83±11.64	1887.98±68.03
–	feb2014	DeepKband2	2.1	10.4	42.4	211.17±2.87	34.27±1.88	1261.76±35.41
3655	feb2014	KbandLargeArea3	2.13	10.35	17.7	185.23±6.35	40.64±3.43	1008.2±37.63
3680	dec2013	mask3	2.18	9.32	5.0	209.49±9.65	14.38±6.1	689.72±36.88
3714	dec2013	mask3	2.18	10.17	66.3	184.03±8.43	72.01±3.47	590.34±27.06
3842	dec2013	mask1	2.1	10.25	8.8	206.85±7.2	19.19±9.42	904.32±33.96
3844	feb2014	DeepKband2	2.44	10.44	N/A	248.01±6.05	38.03±6.42	1655.84±55.51

Table 3 continued

Table 3 *(continued)*

ID	Date	Mask	z_{spec}	M_*	SFR[a]	$V_{2.2}$	σ_g	j_{disk}
3883	dec2013	mask3	2.3	9.12	2.9	87.01±24.22	32.9±13.64	169.18±47.63
4010	feb2014	KbandLargeArea4	2.22	10.07	N/A	105.24±7.93	100.06±4.04	295.17±22.75
4037	dec2013	mask2	2.17	10.77	N/A	307.45±11.23	28.65±9.45	1156.14±45.06
4091	dec2013	mask1	2.1	9.4	3.6	133.45±36.72	62.65±13.94	425.12±117.36
4099	dec2013	mask3	2.44	10.28	N/A	119.92±8.5	16.67±10.01	472.09±37.65
4267	feb2014	KbandLargeArea3	2.41	10.14	N/A	128.02±19.22	46.88±19.41	388.38±59.6
4461	feb2014	DeepKband2	2.3	10.89	10.2	63.69±45.49	101.6±7.37	351.76±251.73
4488	dec2013	mask2	2.31	10.21	7.8	13.41±23.53	126.4±10.4	46.35±81.35
4645	feb2014	DeepKband1	2.1	9.53	5.5	154.04±7.65	13.71±5.65	488.73±25.11
4724	dec2013	mask2	2.3	9.54	3.1	1.42±18.89	56.5±4.74	42.13±561.56
4746	dec2013	mask4	2.18	9.54	6.1	28.37±45.49	56.59±6.91	40.63±65.17
–	feb2014	DeepKband2	2.18	9.54	6.1	58.66±47.28	43.72±5.9	84.02±67.76
4796	feb2014	DeepKband2	2.17	9.45	6.6	30.02±36.87	89.7±7.13	88.28±108.46
4930	feb2014	DeepKband2	2.1	9.46	7.2	110.08±12.99	40.05±8.31	438.98±52.75
5269	dec2013	mask3	2.11	10.03	13.7	176.48±6.07	25.23±6.27	928.94±34.88
5342	dec2013	mask3	2.16	9.06	2.5	84.3±13.09	54.48±8.77	119.25±18.9
5408	dec2013	mask4	2.1	9.74	20.9	180.32±7.71	23.24±17.28	442.28±21.42
5630	feb2014	KbandLargeArea4	2.24	9.97	23.6	179.28±9.08	61.15±3.8	733.62±40.15
5745	feb2014	DeepKband2	2.09	9.15	8.6	41.15±14.31	60.86±2.79	60.21±21.35
5870	dec2013	mask4	2.1	9.9	7.8	118.68±5.07	23.47±3.97	444.18±21.64
6485	dec2013	mask2	2.16	10.41	17.1	182.66±6.08	67.17±6.05	619.32±29.24
6908	feb2014	DeepKband2	2.06	10.47	59.9	395.94±8.19	14.55±6.5	1985.46±43.6
6954	feb2014	DeepKband1	2.13	9.25	6.7	13.28±12.42	17.29±6.82	32.11±30.04
7137	dec2013	mask2	2.16	9.85	9.3	17.32±19.15	83.12±2.37	64.45±71.27
7676	dec2013	mask3	2.16	9.4	4.4	76.67±5.14	39.34±4.75	416.2±29.36
7774	feb2014	DeepKband1	2.2	10.17	10.9	111.81±50.62	95.29±10.76	278.55±126.33
7930	dec2013	mask3	2.1	9.69	8.2	68.3±2.32	58.92±1.79	492.14±28.89
8108	dec2013	mask2	2.16	9.67	6.1	167.71±5.73	48.6±7.88	502.34±23.26
9571	dec2013	mask3	2.09	9.7	7.8	97.75±42.2	66.87±12.8	876.68±383.16

[a]SFR is determined from the Hαflux and corrected for dust assuming a Calzetti et al. (1999) dust law.

We notice a slight difference between the regular and irregular populations in recovered σ_g, where regulars are more likely to have high values of σ_g than irregulars (Figure 5). A logistic regression analysis was inconclusive.

Using our environmentally-diverse sample, our findings are consistent with the results of Simons et al. (2016). In all populations, at low stellar mass, we see evidence of less rotational support. As stellar mass increases, SFGs have increasing amounts of rotational support, no matter their morphology. Despite the large scatter in recovery of simulated $V_{2.2}/\sigma_g$, we can still observe a relation between rotational support and stellar mass.

4.2. *Comparison to Disk-Formation Models*

Table 4. Values for all weighted least-square linear fits[a] to the stellar-mass Tully-Fisher Relation and $S_{0.5}$ Relation and j-$M_\star$ Relation, of the form $\log(y) = A(\log(x) - 10.) + B$

Population	x	y	A	B	B, fixed A[b]	σ_{RMS}	N
Total	M_*	$V_{2.2}$	0.29±0.1	2.19±0.04	2.19±0.04	0.5±0.02	44
Regulars	M_*	$V_{2.2}$	0.28±0.07	2.24±0.03	2.23±0.02	0.6±0.02	25
Irregulars	M_*	$V_{2.2}$	0.3±0.15	2.16±0.06	2.16±0.06	0.39±0.03	19
Total	M_*	$S_{0.5}$	0.38±0.07	2.04±0.03	2.05±0.03	0.15±0.01	44
Regulars	M_*	$S_{0.5}$	0.31±0.05	2.08±0.02	2.08±0.02	0.16±0.01	25
Irregulars	M_*	$S_{0.5}$	0.43±0.1	2.01±0.04	2.03±0.04	0.16±0.01	19
Total	M_*	j	0.36±0.12	2.8±0.05	2.72±0.07	0.52±0.02	44
Regulars	M_*	j	0.39±0.11	2.8±0.05	2.73±0.06	0.56±0.03	25
Irregulars	M_*	j	0.33±0.20	2.81±0.07	2.71±0.11	0.48±0.05	19

[a] Objects more than 3σ away from the fits are rejected from the fits to minimize the influence of outliers.

[b] $A = 0.29$ for the TFR, $A = 0.34$ for $S_{0.5}$, and $A = 0.67$ for j.

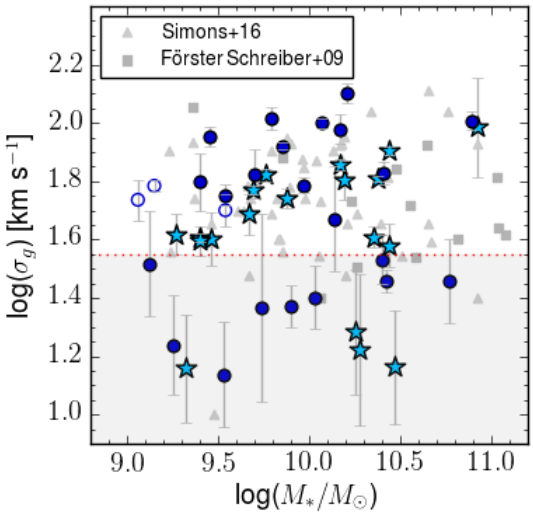

Figure 5. σ_g plotted against $M_\star$, values as determined by HELA models. Colors and markers are as described in Figure 5. Areas below MOSFIRE instrumental resolution are shown in the shaded region, marked by the red dotted line.

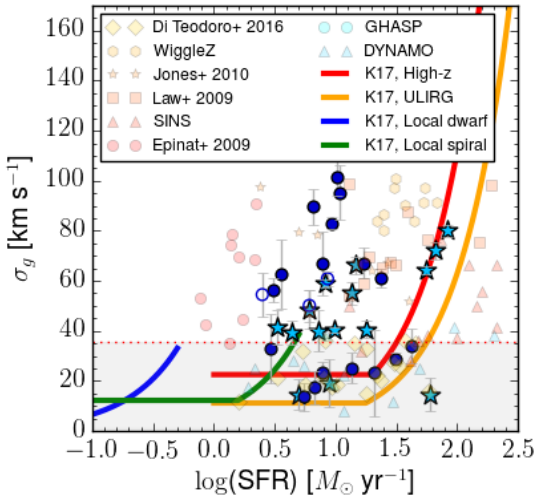

Figure 6. Relationship of our modeled σ_g values against dust-corrected Hα star-formation rate from Tran et al. (2016). We compare our results to the models derived in Krumholz et al. (2017) for local disks and high-z disks. Local and high-z samples with Hα SFRs featured in Krumholz et al. (2017) are also shown here.

Krumholz et al. (2017) introduces a mathematical model for the evolution of gas in the disks of SFGs, which attempts to explain the nature of gas turbulence in these disks. According to this model, gas turbulence can be fed through star formation feedback, radiative transport, or both. The underlying prediction is that in gravitationally unstable galaxies, instability-driven mass transport will move mass inward toward the galaxy center until stability is restored. In this model, disks are never more than marginally gravitationally unstable, and maintain a balance between turbulence driven by star-formation feedback and gravitational instability and the dissipation of tur-

bulence. It predicts that at high redshift, turbulence is mostly gravitationally-driven, whereas in local disks there is a minimum floor of σ_g ($\sim 6-10$ km s^{-1}) where the disks settle that is driven by star-formation feedback.

Our values for σ_g are determined through modeling with HELA, and our star-formation rates (SFR) are determined from dust-corrected Hα flux, assuming a Calzetti et al. (1999) dust law (Tran et al. 2016). In Figure 6, we compare these values to four theoretical models created assuming properties described in Krumholz et al. (2017): a local dwarf (fraction of the ISM in the star-forming phase $[f_{sf}] = 0.2$, rotational velocity at 100km s^{-1}), a local spiral ($f_{sf} = 0.5$, rotational velocity at 200km s^{-1}), a high-redshift galaxy ($f_{sf} = 1.0$, rotational velocity of 200km s^{-1}), and an Ultra-Luminous InfraRed Galaxy (ULIRG, $f_{sf} = 1.0$, rotational velocity of 300km s^{-1}). Our sample maintains a similar shape to the high-z and ULIRG models, but SFRs are lower, perhaps indicating that smaller SFRs can drive turbulence in high-z objects. However, this is consistent with the other high-z observations seen in the text and plotted in Figure 6 (Epinat et al. 2008, 2009b; Förster-Schreiber et al. 2009; Law et al. 2009; Jones et al. 2010; Green et al. 2013; Wisnioski et al. 2015; Stott et al. 2016; Di Teodoro et al. 2016).

The model calculated for a local disk assumes that the dispersion is driven mostly by star-formation feedback, and the ULIRG and high-z models are driven primarily by mass transfer to the core of the galaxy. In this case, it could show that there is more turbulence driven by star formation feedback and mass transfer plays less of a role in high-z galaxies than predicted. Krumholz et al. (2017) assumes these objects are disks and are never more than marginally unstable. The offset of these galaxies from these predictions could mean these objects are unstable and are possibly not even disks. Instead turbulence may be driven at least partially by external factors such as a recent merger or disk instabilities caused by rapid gas accretion.

4.3. *Angular Momenta of SFGs at $z \sim 2$*

Using the maximum rotational velocity (assuming ideal disks, this is $V_{2.2}$), and scale radius, we can estimate specific angular momenta of our galaxies given the formula:

$$j_{disk} = K_n r_s V_{2.2}, \tag{4}$$

where j_{disk} is the specific angular momentum (angular momentum per solar mass), and K_n is defined as

$$K_n = 1.15 + 0.029n + 0.062n^2, \tag{5}$$

where n is the Sérsic index of the galaxy (Romanowsky & Fall 2012). We recognize that in the case of galaxies with complex kinematics and morphological structure, that r_s may not be the best representation of the disk radius, but to obtain a consistent sample we apply this to all galaxies.

Generally angular momentum measurements are taken using IFU spectroscopy. As such, our results may not be the same as what would be measured in an IFU survey. We hope to follow these results up with IFU observations of some of these objects, to determine if the 3D data-cube fitting method yields more accurate measurements of j_{disk} than traditional velocity curve-fitting methods for slit spectroscopy. Despite this disclaimer, our simulated slit observations (Appendix B) demonstrate that we can reliably recover our input j_{disk} to within an offset of -5% (Figure 13). This small offset from our input is consistent over all simulated $\Delta\alpha$, inclination, and sizes, and only becomes unreliable at line masking $> 50\%$ and SNR$<$10.

Additionally, we assume that the angular momentum of the gas disk traces the angular momentum of the stellar disk and older stellar populations. Local kinematic studies usually make

this assumption due to the difficulties of measuring the angular momentum of stellar populations (Romanowsky & Fall 2012; Obreschkow & Glazebrook 2014), and these difficulties increase at high redshift. Simulations show that the stellar disk rotates slower than the gaseous disk in late-type galaxies (El-Badry et al. 2017). In contrast, some observational studies of spatially resolved low-redshift clumpy star-forming disks show that the ionized gas and stellar kinematics are coupled (Bassett et al. 2014). The validity of our assumption is still under debate, but for consistency with local kinematic surveys we apply this assumption.

In Figure 7, left panel, we see our estimated j_{disk} compared to lower-redshift observations. We note a shallower slope than Romanowsky & Fall (2012) at $z = 0$ and KROSS (Harrison et al. 2016) ($z = 0.9$). For the total population, we find a slope of 0.36 ± 0.12 and intercept of 2.80 ± 0.05.

There are no significant differences between regulars and irregulars, although scatter in regulars (0.56 ± 0.03 dex) is higher than irregulars (0.48 ± 0.03). The difference in scatter is due to the slow-rotating low-mass regulars. We see similar slow rotators in the irregular population, but we have fewer in our sample. In both cases, we find a similar, shallow slope of 0.39 ± 0.12 for regulars and 0.33 ± 0.20 for irregulars. The shallow slope is from weighting of our linear fits, since low-rotation objects tend to have higher uncertainties in their measurements. When we perform a linear fit without weighting, we find values much closer to the predicted ($A = 0.63 \pm 0.14$, for the total sample, 0.56 ± 0.15 for regulars, and 0.66 ± 0.27 for irregulars). When we fix $r_t = 1/3 r_s$, we find the slope to move to 0.44 ± 0.12 with no significant differences between irregulars and regulars. We find similar results when $r_t = 0.4 r_s$.

When we hold the slope to be 2/3, we obtain a normalization of 2.72 ± 0.07, which is a normalization offset of 0.12 ± 0.09, or little to no redshift evolution from $z = 0$. This is in conflict with the Harrison et al. (2016) measurement of a 0.3 dex offset from $z = 0$. However if we perform the linear fit without weighting, we find a consistent offset with Harrison et al. (2016). In order to conclusively measure the slope and normalization of the line, we will need to explore the kinematics of low-rotation galaxies with greater precision, to bring these minimize our uncertainties. It is expected that for ΛCDM disks, $\log j \propto \log({M_\odot}^{2/3})$ unless there is mass-dependent angular momentum buildup of the disk (Romanowsky & Fall 2012). If these results are confirmed, it is suggestive that stellar mass has a larger effect on angular momentum than morphology at $z \sim 2$.

Angular momentum is expected to decrease with increasing redshift due to cosmic expansion as

$$j \propto (1+z)^{-1/2}, \tag{6}$$

(Obreschkow et al. 2015). To determine if our sample shows any evolution apart from the theoretical ΛCDM evolution we scale our sample to local galaxies using Equation 6. After correcting for any redshift evolution (Figure 7, right panel), we compare our findings to the work of Burkert et al. (2016). We again see a shallower slope than the $\log j \propto \log({M_\odot}^{2/3})$ trend, but when holding the slope to 2/3 we find an offset with the Burkert et al. (2016) results of 0.12 ± 0.07 dex. If we set r_t to fixed positions relative to r_s, find no significant difference from free r_t. Given the scatter in this relation (0.52 dex), we do not find this to be a significant difference from the Burkert et al. (2016) result, which is not expected to evolve with redshift.

A two-population KS test confirms that to a 95% confidence level, irregular galaxies have higher specific angular momenta than regular galaxies at equivalent stellar mass. Further observations are needed to confirm these results due to low numbers and possible unresolved ir-

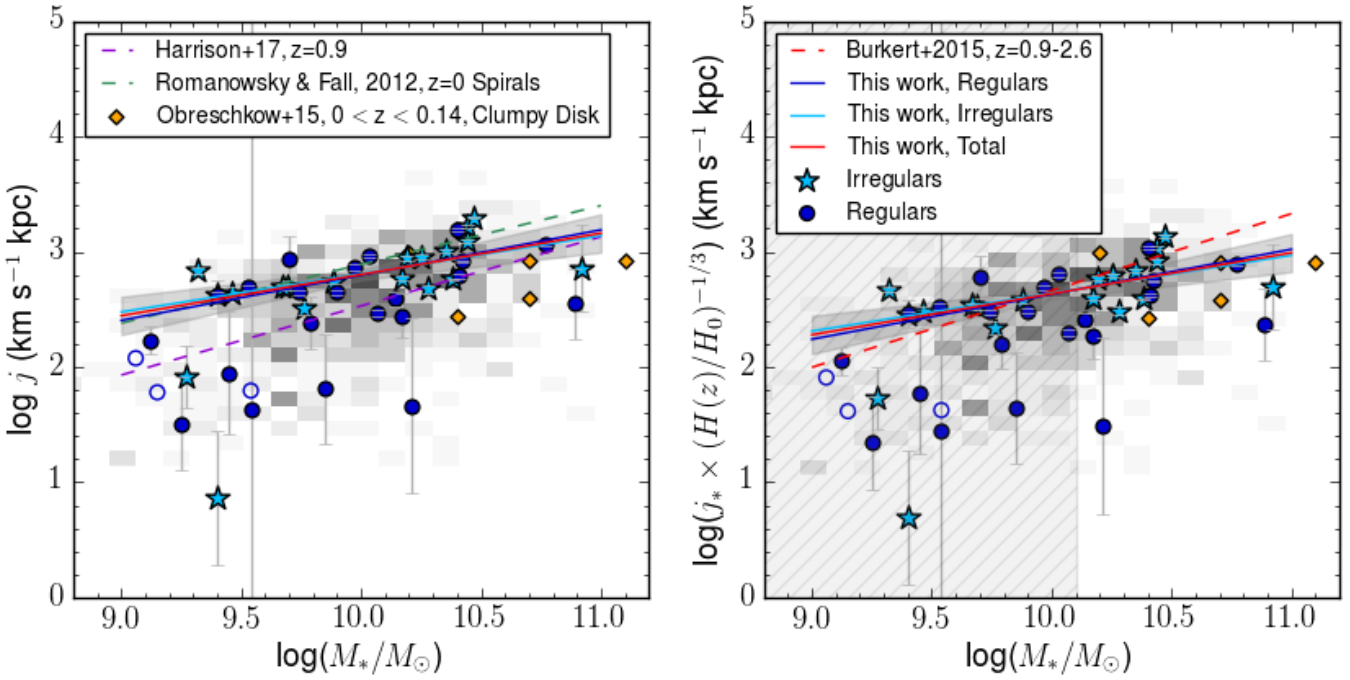

Figure 7. Specific angular momenta of ZFIRE galaxies. Left: Specific angular momenta j against $M_\star$. We compare to the $z = 0.9$ KROSS survey (purple dashed) (Harrison et al. 2016), the $z = 0$ spiral galaxies from Romanowsky & Fall (2012) (green dashed line), and the $z = 0.1$ clumpy, turbulent disk sample of Obreschkow et al. (2015). The shaded squares show the density of objects from the KROSS $z = 0.9$ survey. Right: We correct our values of j for redshift and compare to the results of Burkert et al. (2016) (red dashed). The shaded region shows the mass limit for the selection of galaxies used in the Burkert et al. (2016) sample.

regular structure in regular galaxies. Most of this offset is on the low-mass ($M_\star$<10) end of the j-$M_\star$relation, on the high-mass end ($M_\star$>10) these relationships tighten. When low-rotation resolved objects are removed, the irregular and regular populations are not significantly different.

Additionally, we compare our sample to the clumpy, turbulent galaxies of Obreschkow et al. (2015), often considered high redshift analogs in the local universe. We can confirm that at least kinematically, $z \sim 2$ galaxies have similar properties to these local galaxies.

5. DISCUSSION

5.1. *Morphology and Kinematics*

In some cases it appears that irregulars, including merger candidates, show ordered rotation fields, and as such cannot be identified by kinematics alone. This is also observed in the IFU-based work of KMOS Deep Survey (KDS) (Turner et al. 2017), who describe a similar phenomenon of merger candidates with ordered rotation fields. In Hung et al. (2015) local merging galaxies are artificially redshifted and their rotation is examined. All mergers with the exception of those with strong tidal features and two nuclei showed ordered rotation fields. This could explain the similarity of the kinematic scaling relations for regular and irregular galaxies, which could include mergers, derived in our results. We demonstrate that our irregular galaxies are often well-described by ordered rotation, as our models are derived from rotation-dominated isolated galaxies, and our kinematic extractions assume ordered rotation.

However as irregular galaxies are not well described by photometric modeling (Figure 1),

these measurements could be incorrect from assuming that our morphological and kinematic PAs are consistent, and that our intrinsic axis ratio is 0.18. Similarly, in our modeling, we assume that all galaxies are infinitely thin disks with Sérsic indices of 1, which is not true for most of our measured galaxies, and for irregular galaxies, the Sérsic profile is unreliable.

Given these caveats in our analysis, we expect different behaviors in our kinematic relationships if growth is dominated by major mergers or smooth gas accretion. Mergers, depending on the geometry of the system, could cause a system to abruptly gain or lose angular momentum, and would increase the scatter around kinematic scaling relations (Vitvitska et al. 2002; Naab et al. 2014; Rodriguez-Gomez et al. 2017). Assuming that these mergers are not happening in a preferred direction, we would expect a larger scatter in our velocity and angular momentum relations in merging galaxies (which we are assuming are represented by irregulars). We would also expect these galaxies to have higher values for σ_g than galaxies that have not undergone a recent merger.

If growth is dominated by smooth accretion, the angular momentum of galaxies would again be subject to the direction of gas falling onto the disk. If gas is accreted along a filament, it would exert a torque causing an increase in angular momentum (White 1984; Keres et al. 2004; Sales et al. 2012).

Kinematic surveys are often biased toward galaxies with ordered rotation and a relatively small contribution of σ_g toward overall kinematics at an observed redshift. This is partially because these galaxies are usually intrinsically brighter, as they are more massive. In addition to brightness, the size of a galaxy can have an effect on its kinematics. Newman et al. (2012) demonstrated that spatially unresolved galaxies in kinematics surveys can have underestimated rotational velocities. In our sample, we rejected four compact galaxies with unreliable measurements for $V_{2.2}$. This could bias our sample and our results, underestimating the prevalence of low $V_{2.2}/\sigma_g$ galaxies. Additionally, we could be classifying galaxies with unresolved irregular structure as regular galaxies.

We find similar levels of scatter between regular and irregular populations in the TFR, $S_{0.5}$, (Figure 3) and j_{disk} relations, but irregular galaxies have higher j_{disk} values at given stellar mass (Figure 7), and do not have higher values of σ_g (Figure 5). Due to our limited sample, more observations are needed to confirm these results. Given that these galaxies have clear irregularities and sometimes show obvious signs of merging close companions, these results are puzzling. We have yet to find simulations which show results like our observations.

In the case that irregulars have higher j_{disk} than regular galaxies, a significant portion of our sample is in an over-dense proto-cluster region, and this may affect the direction of gas infall or orientation of mergers. Our assumption was that in the case of merger-dominated or accretion-dominated growth, orientation would be random, and would create a stochastic scatter. However it is possible that these interactions may have a preferred orientation, possibly due to the filamentary structure of the cosmic web (Keres et al. 2004; Sales et al. 2012; Stewart et al. 2013; Danovich et al. 2015). More observations are needed for a robust analysis of our conjecture, and knowledge of the cosmic web surrounding this structure would be beneficial.

5.2. *The Reliability of Kinematics From Slit Spectroscopy*

Some of the scatter in our kinematic scaling relations and angular momentum is possibly related to the scatter in our ability to recover our simulated V_{rot} and σ_g, and the inherent issues with recovering velocities in unresolved galaxies. This was likely because in unresolved emission lines, the position of the turnover radius

is unclear, so we tend to overestimate the positions of simulated r_t and V_t. In other surveys, it is assumed $r_t = 0.4r_s$, as observed in Miller et al. (2011). However, this is an empirical observation at $z \sim 1.7$, when disks are settling. Whether this assumption holds at $z > 2$ is unclear, but the position of r_t in an arctangent velocity curve will affect the derived rotational velocities of a galaxy.

Our simulations (Appendix B) demonstrate that we tend to consistently overestimate $V_{2.2}$ by around 10% at high data quality (Appendix B.1) and inclination $> 25^o$ (Figure 11). When we can fix r_t to a known value, our recovery is more accurate, to 5%. Similarly we underestimate σ_g by 10%. Small deviations from our inputs in either of these values lead to overestimated values for $V_{2.2}/\sigma_g$ with a high scatter in recovered values of our simulations, meaning recovered $V_{2.2}/\sigma_g$ values may be unreliable (Figure 12). However, these offsets lead to only slightly overestimated values for $S_{0.5}$, which are reliably offset at high data quality and inclination $> 25^o$. Similarly, our recovery of j_{disk} is reliable within 5% of the input with small scatter in our results (Figure 13). These results show that given the degeneracies seen in modeling emission lines from slit spectroscopy, we can reliably recover values for $S_{0.5}$ and j_{disk} if these offsets are accounted for.

We suggest that current slit observations and data analysis can reliably measure $S_{0.5}$ and specific angular momentum of spatially resolved galaxies at $z \sim 2$. Unresolved galaxies can give unreliable velocity measurements, so increased spatial resolution in multi-object spectrographs are necessary to progress in our understanding of high-redshift kinematics. The James Webb Space Telescope (JWST) will benefit kinematics due to the NIRSPEC instrument for this reason. NIRSPEC shutter resolution will be at $0.1''$, but more importantly these data will not be seeing-limited. Multi-object slit spectroscopy and JWST provide the opportunity for larger sample sizes, and increased sensitivity to low-mass and faint objects. As we enter the era of large astronomical surveys, slit spectroscopy will prove an invaluable tool for building large samples of galaxies.

6. SUMMARY

We examine an environmentally diverse sample of $z \sim 2$ star-forming galaxies in the COSMOS field observed by the ZFIRE survey. Complementary NIR imaging in the F160W bandpass from HST/WFC3 as part of the CANDELS project allow for morphological analysis of this sample. This sample is made up of 44 galaxies: 14 are associated with an over-dense region at $z = 2.095$ and 30 are in the field from $2.0 < z < 2.5$. These galaxies are split into two morphological sub-samples, termed "regulars" (25) and "irregulars" (19) (Figure 1). This classification is based on the presence of excess residual emission from a single-Sérsic fit where a galaxy is classified as an irregular if residual levels are above twice the nearby sky levels, and greater than 25% of the original flux levels.

The Hα emission lines are used to extract kinematic components using HELA (Straatman in prep). HELA simulates a 3D data cube, collapses it into a $0.7''$ slit, and runs an MCMC simulation to determine the best-fit model to the emission line, assuming an arctangent rotation curve and a constant gas velocity dispersion. HELA recovers the velocity of simulated galaxies (Appendix B) at $2.2r_s$ ($V_{2.2}$) to within 10% of our input and σ_g to within -10% of its input (Figure 11). Using recovered kinematics, HELA can reliably recover $S_{0.5}$ to a minor offset of within -10% of the input, and j_{disk} (specific angular momentum) to within -5% of the input (Figures 12 and 13). $V_{2.2}/\sigma_g$ tends to be overestimated by 30% with a high scatter in recovery. When we constrain the location of the kinematic turnover radius r_t to a known position relative

to the scale radius r_s, our offsets decrease by 5% from inputs.

Using the values for $V_{2.2}$ derived from our fitting method, we determine a stellar-mass TFR of $\log(V_{2.2}) = (0.29 \pm 0.1)\log(M/M_\odot - 10) + (2.19 \pm 0.04)$ (Figure 3). There are no significant differences between regulars and irregulars. When we include the contribution of σ_g, in the case of $S_{0.5}$, we find $\log(S_{0.5}) = (0.38 \pm 0.07)\log(M/M_\odot - 10) + (2.04 \pm 0.03)$. The scatter of the overall sample is consistent with other measurements of $S_{0.5}$ at $z > 1.5$ (Price et al. 2015; Straatman et al. 2017).

To measure pressure against rotational support, we determine $V_{2.2}/\sigma_g$ (Figure 4), and measure a trend of increasing rotational support with increasing stellar mass, similar to the results of Simons et al. (2016). However there is high scatter in our recovery of simulated $V_{2.2}/\sigma_g$values, leading us to believe that the significant scatter in our results (0.6 dex) may be driven by measurement uncertainties.

We compare our results to the mathematical modeling of Krumholz et al. (2017), which are based on a balance between turbulence driven by star-formation feedback and gravitational instability, and the dissipation of turbulence by mass transport (Figure 6). Our sample shows a similar shape in the dust-corrected SFR and $\sigma_g$turbulence but the models overpredict the SFR necessary to produce high gas turbulence in high redshift galaxies.

We also estimate specific angular momentum values (Figure 7), and determine that galaxies have a shallower relationship (slope $A = 0.36 \pm 0.12$) between j_{disk} and $M_\star$ than predicted ($A = 0.67$), either due to undersampling low-rotation low-mass galaxies, or due to a mass-dependent angular momentum buildup in the disk (Romanowsky & Fall 2012). Additionally, we do not find any evidence of angular momentum offsets with redshift at consistent stellar mass. More observations of these galaxies will clarify our results, as well as more precise measurements of the kinematics of pressure-dominated SFGs. Our irregular and regular populations were consistent. Our simulated observations demonstrate reliable recovery of input kinematics, and we achieve similar j_{disk} measurements to $z \sim 0.1$ high-z analogs (Obreschkow et al. 2015).

Our work demonstrates that slit spectroscopy can reliably recover kinematics measurements such as $V_{2.2}$, $S_{0.5}$, or j_{disk} to either a consistent offset that can be corrected, or to a small offset from simulated inputs. Low spatial resolution can limit our ability to recover kinematics, but with an increase in resolution, MOS spectroscopy can provide robust kinematic measurements. In the coming age of large astronomical datasets, the reliability of slit spectroscopy will be instrumental in building large spectroscopic samples at high redshift and using the Near Infrared Spectrograph, NIRSPEC on the James Webb Space Telescope.

We would like to thank the anonymous referee who provided helpful comments and suggestions, greatly improving our analysis of this work. We acknowledge S. Kassin, J. Walsh, and R. Quadri for helpful conversations, and the Mitchell family, particularly the late George P. Mitchell, for their continuing support of astronomy. L. Alcorn thanks the LSSTC Data Science Fellowship Program, her time as a Fellow has benefited this work. This work was supported by a NASA Keck PI Data Award administered by the NASA Exoplanet Science Institute. Data presented herein were obtained at the W. M. Keck Observatory from telescope time allocated to NASA through the agency's scientific partnership with the California Institute of Technology and the University of California. This work is supported by the National Science Foundation under Grant #1410728. GGK acknowledges the support of the Australian Research

Council through the award of a Future Fellowship (FT140100933). The authors acknowledge the Texas A&M University Brazos HPC cluster that contributed to the research reported here.

The authors wish to recognize and acknowledge the very significant cultural role and reverence that the summit of Mauna Kea has always had within the indigenous Hawaiian community. We are most fortunate to have the opportunity to conduct observations from this mountain.

REFERENCES

Alcorn, L. Y., Tran, K.-V. H., Kacprzak, G. G., et al. 2016, Astrophys. J., 825, L2
Bassett, R., Glazebrook, K., Fisher, D. B., et al. 2014, 18
Bekiaris, G., Glazebrook, K., Fluke, C. J., & Abraham, R. 2015, 30, 1
Bruzual, G., & Charlot, S. 2003, Mon. Not. R. Astron. Soc., 344, 1000
Burkert, A., Forster-Schreiber, N. M., Genzel, R., et al. 2016, arXiv.org, 1510, 3262
Calzetti, D., Armus, L., Bohlin, R. C., et al. 1999, 20, 27
Capak, P., Aussel, H., Ajiki, M., et al. 2007, Astrophys. J. Suppl. Ser., 172, 99
Chabrier, G. 2003, Publ. Astron. Soc. Pacific, 115, 763
Cortese, L., Fogarty, L. M., Bekki, K., et al. 2016, Mon. Not. R. Astron. Soc., 463, 170
Cowley, M. J., Spitler, L. R., Tran, K. V. H., et al. 2016, Mon. Not. R. Astron. Soc., 457, 629
Cresci, G., Hicks, E. K. S., Genzel, R., et al. 2009, Astrophys. J., 697, 115
Daddi, E., Bournaud, F., Walter, F., et al. 2010, ApJ, 713, 686
Danovich, M., Dekel, A., Hahn, O., Ceverino, D., & Primack, J. 2015, Mon. Not. R. Astron. Soc., 449, 2087
Di Teodoro, E. M., Fraternali, F., & Miller, S. H. 2016, arXiv:1602.04942
El-Badry, K., Quataert, E., Wetzel, A., et al. 2017, 23, 1
Emsellem, E., Cappellari, M., Krajnović, D., et al. 2007, Mon. Not. R. Astron. Soc., 379, 401
Epinat, B., Amram, P., & Marcelin, M. 2008, Mon. Not. R. Astron. Soc., 390, 466
Epinat, B., Contini, T., Fevre, O. L., et al. 2009a, Astron. Astrophys., 504, 789
—. 2009b, 805, 23
Fall, S. M., & Efstathiou, G. 1980, Mon. Not. R. Astron. Soc., 193, 189
Foreman-Mackey, D., Hogg, D. W., Lang, D., & Goodman, J. 2012, 1
Förster-Schreiber, N. M., Genzel, R., Bouche, N., et al. 2009, 3, 81
Freeman, K. C. 1970, Astrophys. J., 160, 811
Glazebrook, K. 2013, eprint arXiv, 1305, 2469
Green, A. W., Glazebrook, K., McGregor, P. J., et al. 2013, Mon. Not. R. Astron. Soc., 437, 1070
Grogin, N. A., Kocevski, D. D., Faber, S. M., et al. 2011, Astrophys. J. Suppl. Ser., 197, 35
Harrison, C. M., Johnson, H. L., Swinbank, A. M., et al. 2016, 18, 1
Hung, C.-L., Rich, J. A., Yuan, T., et al. 2015, Astrophys. J., 803, 62
Jones, T. a., Swinbank, a. M., Ellis, R. S., Richard, J., & Stark, D. P. 2010, Mon. Not. R. Astron. Soc., 404, 1247
Kacprzak, G. G., Yuan, T., Nanayakkara, T., et al. 2015, Astrophys. J., 802, L26
Kacprzak, G. G., van de Voort, F., Glazebrook, K., et al. 2016, arXiv:1607.00014
Kassin, S. a., Weiner, B. J., Faber, S. M., et al. 2007, Astrophys. J., 660, L35
Keres, D., Katz, N., Weinberg, D. H., & Dave, R. 2004, 000, arXiv:0407095
Kewley, L. J., Glazebrook, K., Spitler, L., & Cowley, M. 2015, arXiv:arXiv:1506.07525v1
Koekemoer, A. M., Faber, S. M., Ferguson, H. C., et al. 2011, Astrophys. J. Suppl. Ser., 197, 36
Kriek, M., van Dokkum, P. G., Labbe, I., et al. 2009, 2, arXiv:0905.1692
Krumholz, M. R., Burkhart, B., Forbes, J. C., & Crocker, R. M. 2017, 000, arXiv:1706.00106
Lagos, C. d. P., Theuns, T., Stevens, A. R., et al. 2017, Mon. Not. R. Astron. Soc., 464, 3850
Law, D. R., Steidel, C. C., Erb, D. K., et al. 2009, 34
McLean, I. S., Steidel, C. C., Epps, H. W., et al. 2012, Ground-based Airborne Instrum. Astron. IV. Proc. SPIE, 8446, 84460J

Miller, S. H., Bundy, K., Sullivan, M., Ellis, R. S., & Treu, T. 2011, 115, 22
Mo, H. J., Mao, S., & White, S. D. M. 1997, ArXiv Astrophys. e-prints, 13
Naab, T., Oser, L., Emsellem, E., et al. 2014, Mon. Not. R. Astron. Soc., 444, 3357
Nanayakkara, T., Glazebrook, K., Kacprzak, G., et al. 2016, Astrophys. J., 828, 1
Nanayakkara, T., Glazebrook, K., Kacprzak, G. G., et al. 2017, arXiv:1703.04536
Newman, S. F., Genzel, R., Förster-Schreiber, N. M., et al. 2012, Astrophys. J., 761, 43
Obreschkow, D., & Glazebrook, K. 2014, Astrophys. J., 784, 26
Obreschkow, D., Glazebrook, K., Kilborn, V., & Lutz, K. 2016, Astrophys. J. Lett., 824, 1
Obreschkow, D., Glazebrook, K., Bassett, R., et al. 2015, 3, 1
Peng, C. Y., Ho, L. C., Impey, C. D., & Rix, H.-W. 2010, Astron. J., 139, 2097
Penoyre, Z., Moster, B. P., Sijacki, D., & Genel, S. 2017, 26, 1
Price, S. H., Kriek, M., Shapley, A. E., et al. 2015, arXiv:1511.03272
Puech, M., Hammer, F., Lehnert, M. D., & Flores, H. 2007, a&a, 466, 83
Reyes, R., Mandelbaum, R., Gunn, J. E., Pizagno, J., & Lackner, C. N. 2011, 2347–2386, arXiv:1106.1650
Rodriguez-Gomez, V., Sales, L. V., Genel, S., et al. 2017, Mon. Not. R. Astron. Soc., 467, 3083
Romanowsky, A. J., & Fall, S. M. 2012, 17, arXiv:1207.4189
Sales, L. V., Navarro, J. F., Theuns, T., et al. 2012, Mon. Not. R. Astron. Soc., 423, 1544
Simons, R. C., Kassin, S. A., Trump, J. R., et al. 2016, 21
Simons, R. C., Kassin, S. A., Weiner, B. J., et al. 2017, arXiv:1705.03474
Skelton, R. E., Whitaker, K. E., Momcheva, I. G., et al. 2014, arXiv:1403.3689
Spitler, L. R., Labbé, I., Glazebrook, K., et al. 2011, 1
Stewart, K. R., Brooks, A. M., Bullock, J. S., et al. 2013, Astrophys. J., 769, 1
Stott, J. P., Swinbank, A. M., Johnson, H. L., et al. 2016, arXiv:1601.03400
Straatman, C. M. S., Spitler, L. R., Quadri, R. F., et al. 2016, 39
Straatman, C. M. S., Glazebrook, K., Kacprzak, G. G., et al. 2017, 1
Straatman, Caroline M. S., e. a. in prep
Swinbank, M., Smail, I., Sobral, D., et al. 2012, ApJ, 760, 130
Tacconi, L. J., Genzel, R., Neri, R., et al. 2010, arXiv, 1002, 2149
Tran, K.-V. H., Nanayakkara, T., Yuan, T., et al. 2015, 1
Tran, K.-V. H., Alcorn, L. Y., Kacprzak, G. G., et al. 2016, 1
Tully, R. B., & Fisher, J. R. 1977, Astron. Astrophys., 54, 661
Turner, O. J., Cirasuolo, M., Harrison, C. M., et al. 2017, 31, 1
van der Wel, a., Franx, M., van Dokkum, P. G., et al. 2014, Astrophys. J., 788, 28
Vitvitska, M., Klypin, a. a., Kravtsov, a. V., et al. 2002, Astrophys. J., 581, 11
Weiner, B. J., Willmer, C. N. a., Faber, S. M., et al. 2006, Astrophys. J., 653, 1049
White, S. D. M. 1984, Astrophys. J., 286, 38
White, S. D. M., & Rees, M. J. 1978, Mon. Not. R. Astron. Soc., 183, 341
Wisnioski, E., Förster Schreiber, N. M., Wuyts, S., et al. 2015, Astrophys. J., 799, 209
Yuan, T., Nanayakkara, T., Kacprzak, G. G., et al. 2014, Astrophys. J., 795, L20

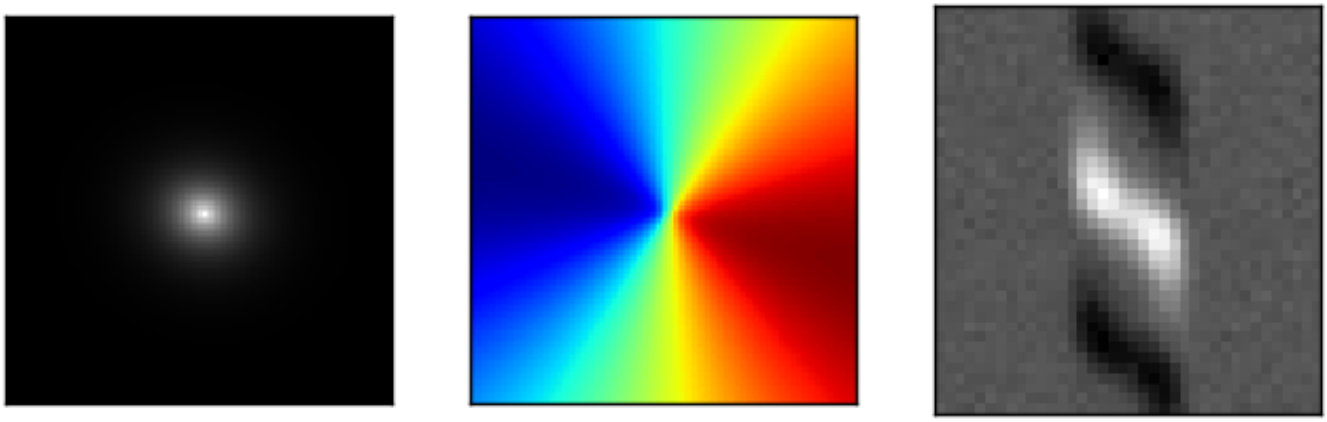

Figure 8. An example of our models created in HELA. Left: Spatial intensity profile of an infinitely thin disk galaxy, with $V_t = 300$ km s^{-1}, $r_s = 0.5''$, $r_t = 0.15''$, σ_g= 25 km s^{-1}, $i = 30^o$, and $\Delta\alpha = 15^o$. Center: The line of sight velocity field of the galaxy to the left. Right: Emission line of the galaxy described, convolved with a 2D Moffat profile at $0.7''$ seeing.

APPENDIX

A. HELA MODELING

Here we describe our method of fitting our emission lines, using HELA (Heidelberg Emission Line Algorithm), provided by its developer, C.M. Straatman (Straatman in prep), which uses the prescription of Price et al. (2015).

The emission line fit is generated from a 3D data-cube. This data cube is generated given an input inclination, slit offset, redshift, emission line wavelength, and an estimated scale radius, turnover radius, asymptotic velocity, and σ_g. Given bounds in spatial and wavelength space (x_{init} and y_{init}), we create an x-y grid of velocity space, face-on with a galaxy, or at $i = 0^o$. With our input $\Delta\alpha$, we transform our model using

$$x_0 = x_{init} \cos\Delta\alpha - y_{init} \sin\Delta\alpha \tag{A1}$$

$$y_0 = x_{init} \sin\Delta\alpha + y_{init} \cos\Delta\alpha, \tag{A2}$$

to account for our offset between the galaxy major axis and our slit PA. We transform our values using our input inclination with

$$x_i = x_p / \cos i, \tag{A3}$$

rotating our galaxy into its correct inclination. We define a variable r, the distance from the center of the galaxy, as,

$$r^2 = \sqrt{x_i^2 + y_0^2}, \tag{A4}$$

and the angle ψ as,

$$\cos\psi = y_p / r. \tag{A5}$$

A velocity profile is created assuming an infinitely thin disk, an arctangent rotation curve

$$V_{rot}(r) = \frac{2}{\pi} V_t \; arctan \frac{r}{r_t}, \tag{A6}$$

where V_t is the asymptotic velocity and r_t is the turnover radius. This equation is then used to determine the line-of-sight velocity (V_{LOS})

$$V_{LOS} = V_{rot}(r) \sin i \cos \psi. \tag{A7}$$

To map our kinematic components into a 2D emission-line observation, as would be seen from slit spectroscopy, we create a spatial exponential intensity profile,

$$I(r) = I_0 \exp \frac{-(r)}{r_s}, \tag{A8}$$

where r_s is the intensity scale radius. The intensity profile is then mapped onto V_{LOS} using

$$I(r, \lambda) = \frac{I(r)}{\sqrt{2\pi}\sigma_g} \exp(-\frac{(\lambda - \lambda_{LOS})^2}{2\sigma_g^2}), \tag{A9}$$

where σ_g is the intrinsic gas velocity dispersion.

We convolve this intensity profile with a Moffat 2D PSF if Moffat parameters α and β are provided, as in the Moffat PSF profile:

$$PSF(r) = \frac{\beta - 1}{\pi \alpha^2} \left[1 + \left(\frac{r}{\alpha} \right)^2 \right]^{-\beta}. \tag{A10}$$

If Moffat parameters are not provided, then a Gaussian profile of given seeing can be used in place of a Moffat profile. Then we collapse the model over a slit width of 0.7″, and scale to our preferred intensity signal. During fitting to MOSFIRE data or simulated observations, this scaling is determined from a weighted least-squares fit of the model to the data or simulation, weighted by the measurement errors from the weight images.

Our best-fit models for our sample can be seen in Figure 9.

B. FITTING SIMULATED EMISSION LINES

We test our fitting procedure on a sample set of simulated MOSFIRE observations. We use 1000 simulated emission lines of galaxies created from the GBKFIT program (Bekiaris et al. 2015). Three examples of these simulated emission lines are in Figure 4.

GBKFIT creates simulated 3D data cubes of galaxies given initial properties such as galaxy redshift (z), scale length r_s (1-5 kpc), turnover radius r_t ($\frac{r_s}{3}$), turnover velocity V_t (100-400 km s^{-1}), gas sigma σ_g (20-100 km s^{-1}), inclination i (0-90^o), and offset from the PA of the slit $\Delta\alpha$ (-45-45^o). Galaxies are all infinitely thin exponential disks with arctangent rotation curves,

$$V_{rot}(r) = \frac{2}{\pi} V_t \; arctan \frac{r}{r_t}. \tag{B11}$$

All objects have a constant intrinsic gas velocity dispersion. These models are convolved with the desired seeing and projected through a 0.7″ wide slit. In this case, we used 2D Moffat at 0.7″ seeing

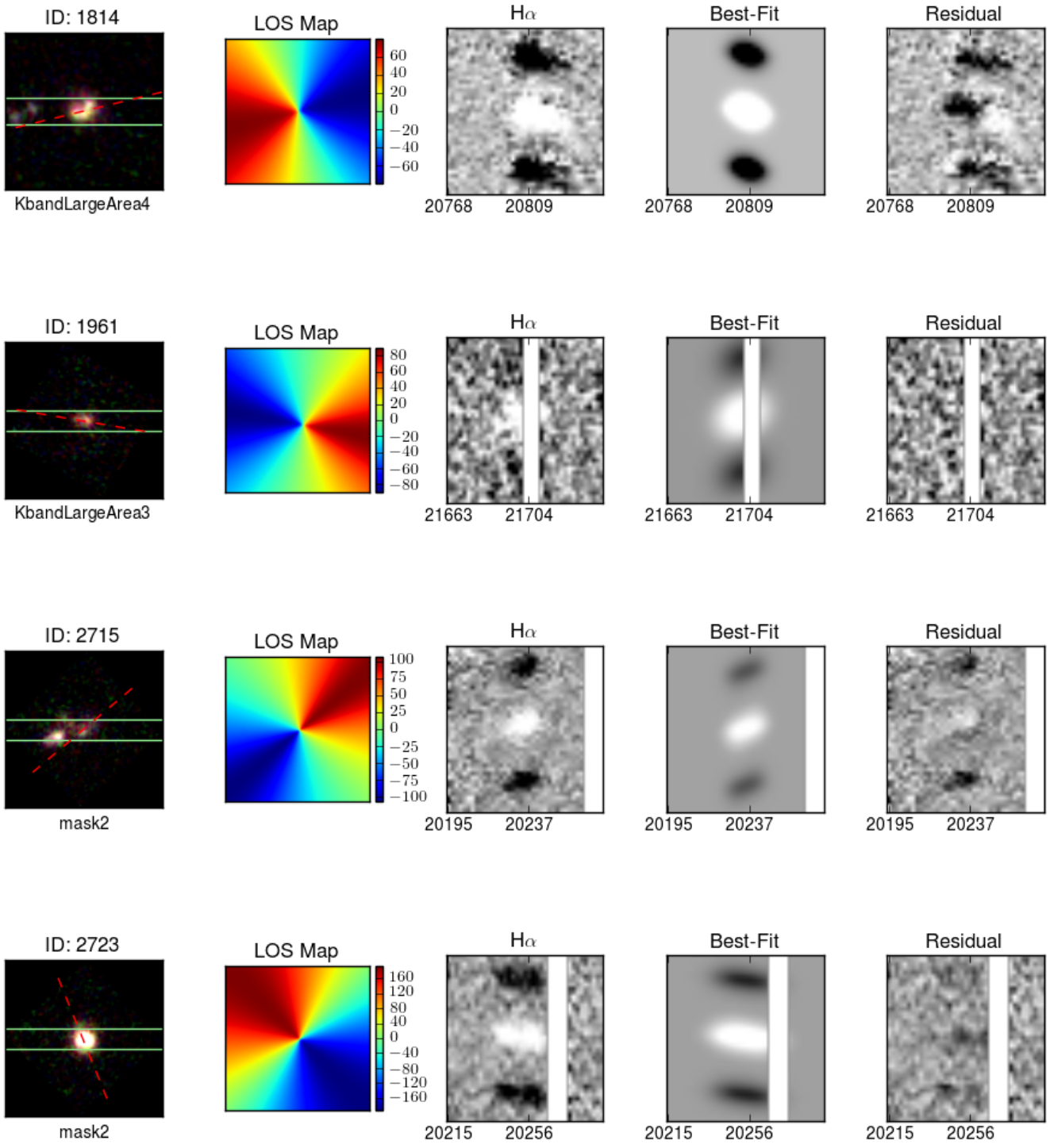

Figure 2. Imaging and best fits of galaxies in our sample. From Left: RGB images are from F160W (red), F140W (green), and F125W (blue). The slit overlay is shown in green and the major axis of the galaxy is shown in red. Second from left: The LOS map is aligned with the RGB image. Center: The Hα emission line with sky emission masked in white and continuum removed, if present. Second from right: Best-fit emission line from HELA modeling, characterized by the LOS map. Right: Residual from the best-fit line.

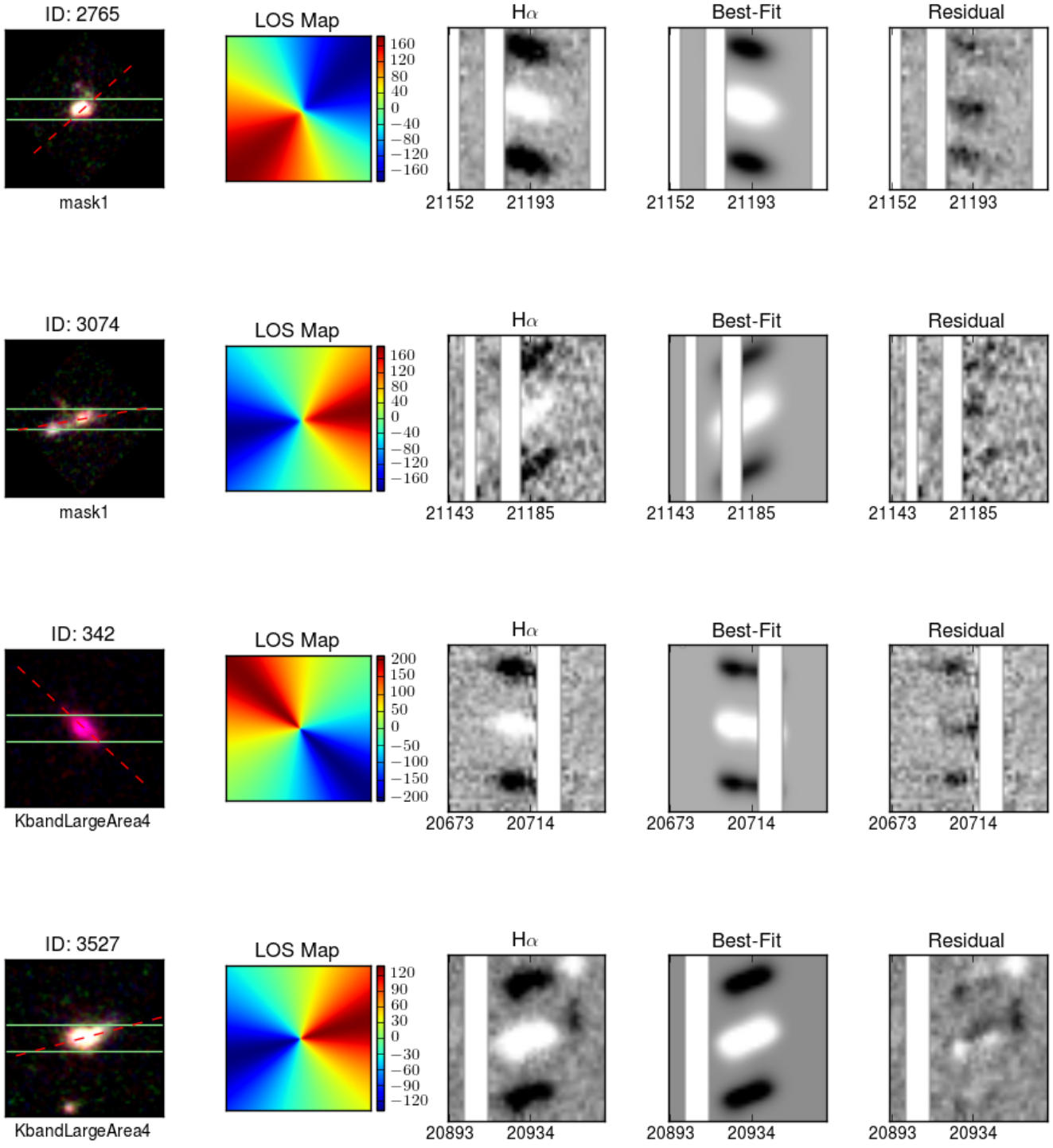

Figure 2. Continued

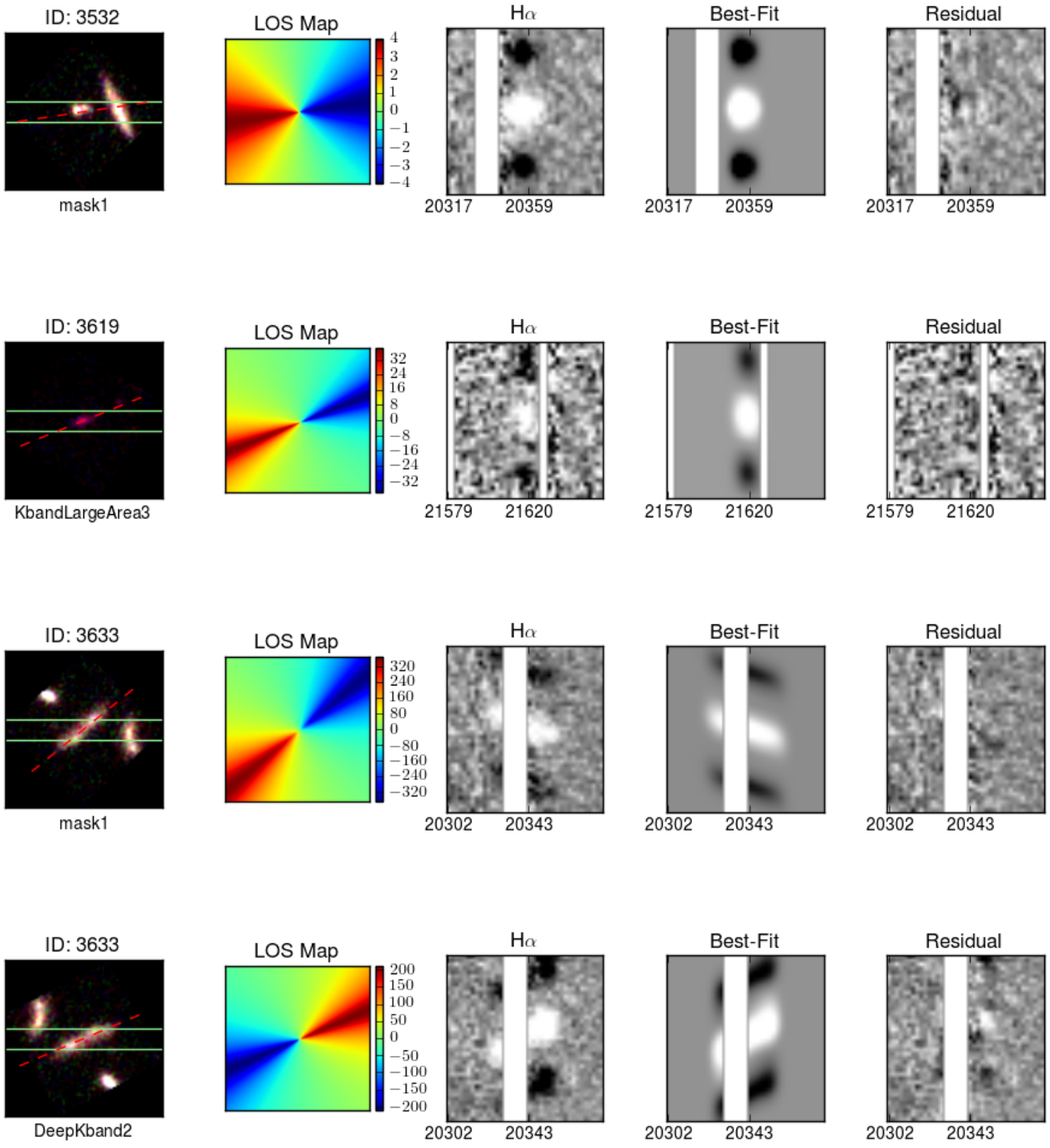

Figure 2. Continued

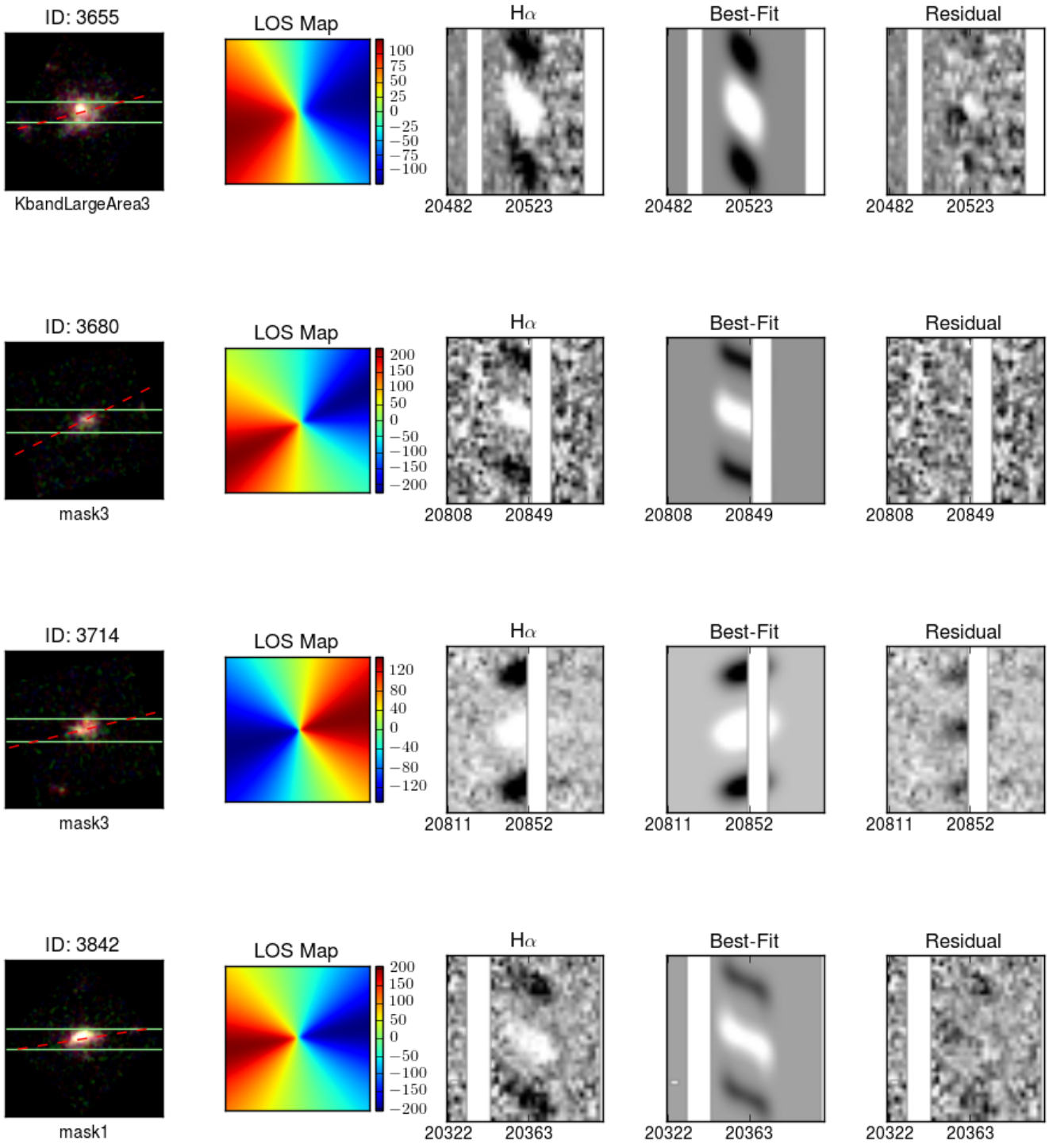

Figure 2. Continued

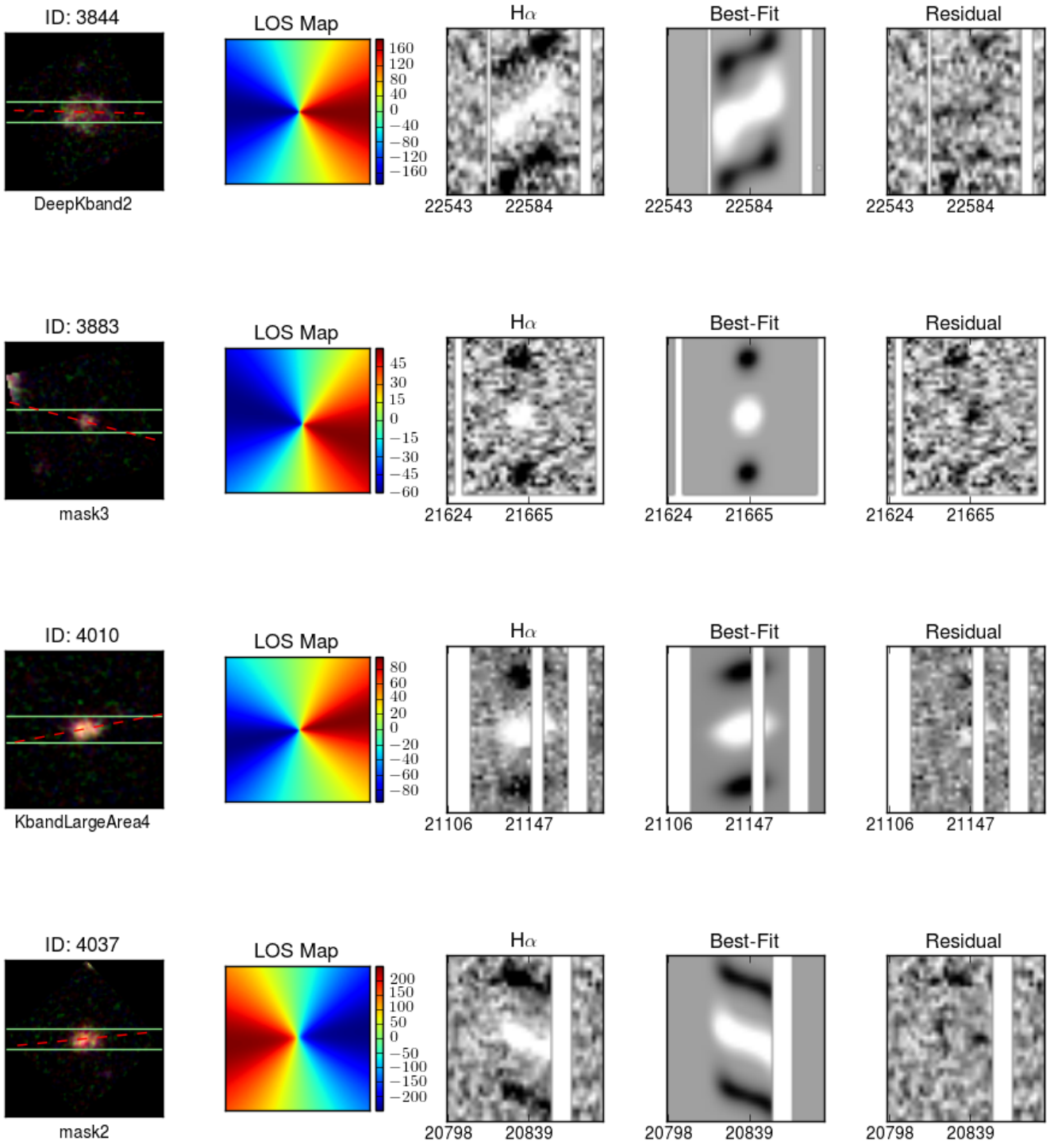

Figure 2. Continued

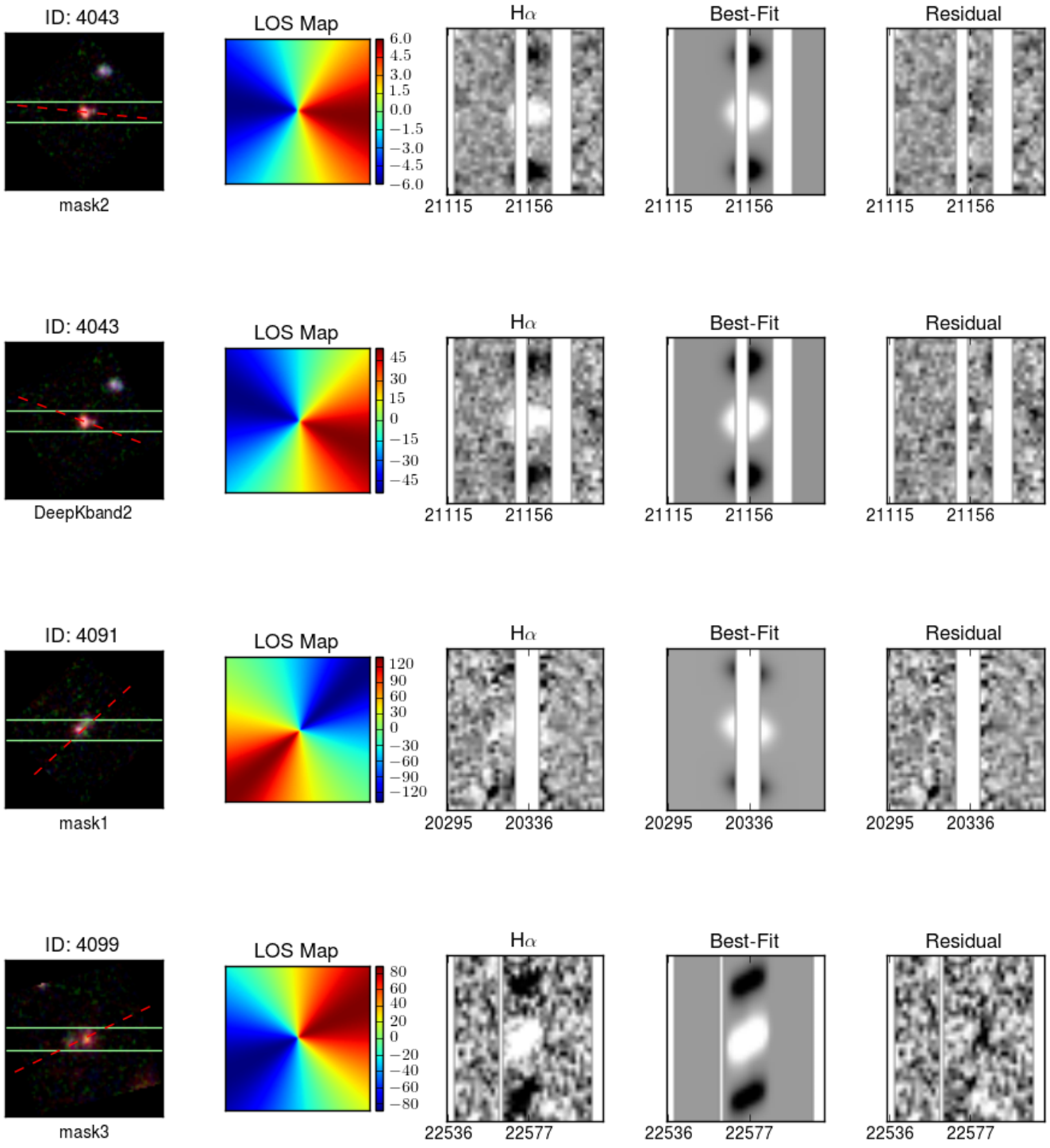

Figure 2. Continued

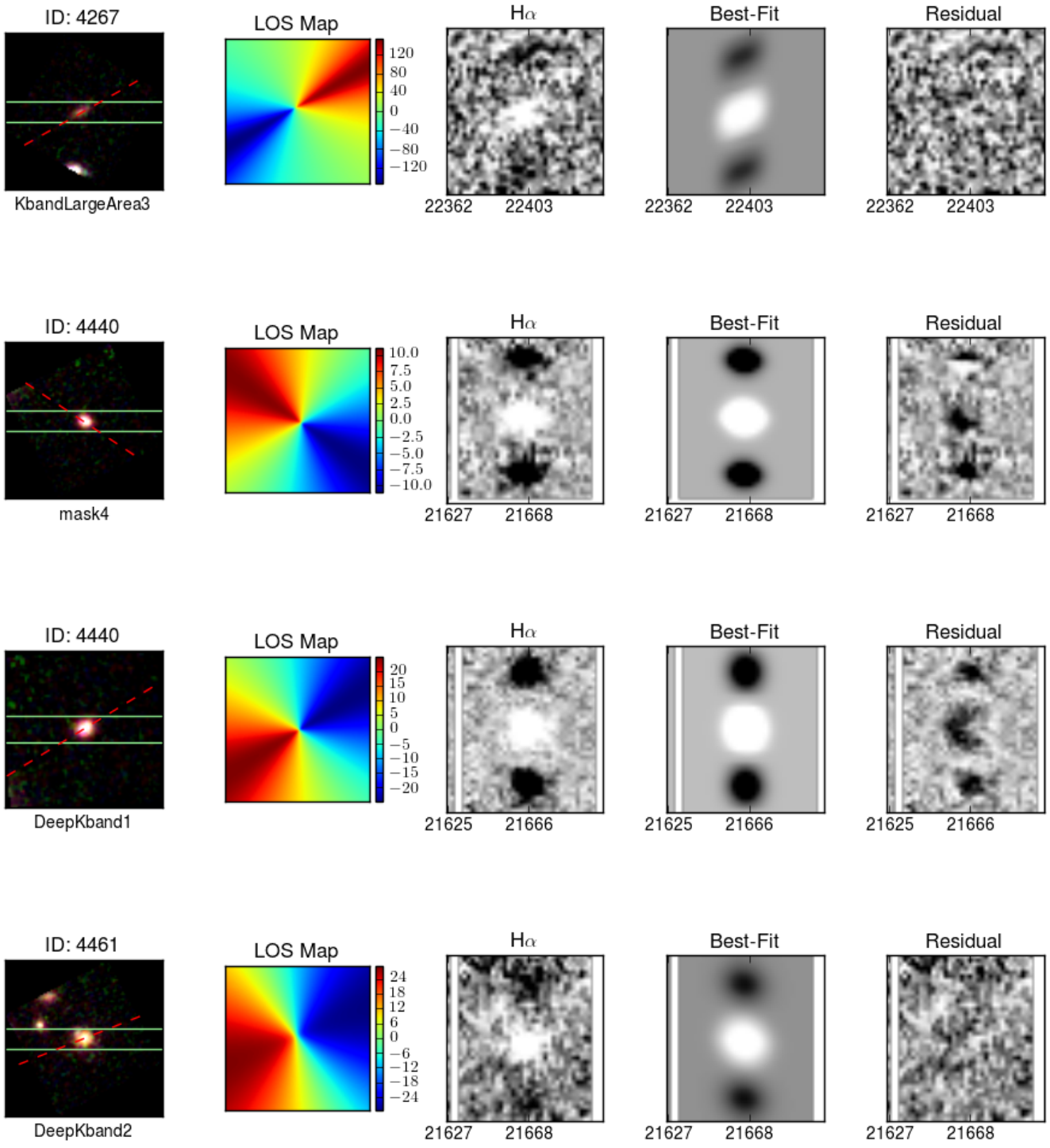

Figure 2. Continued

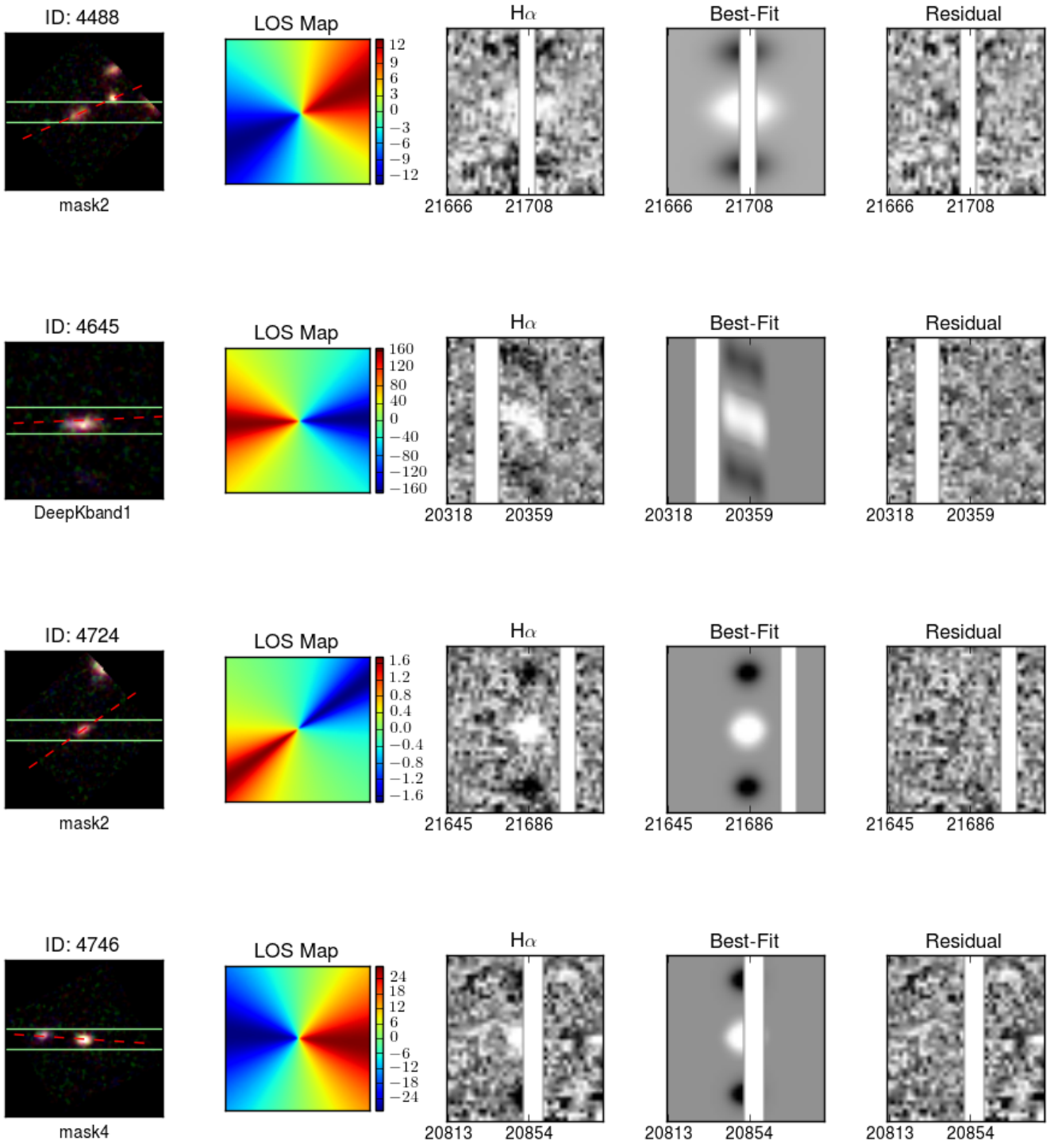

Figure 2. Continued

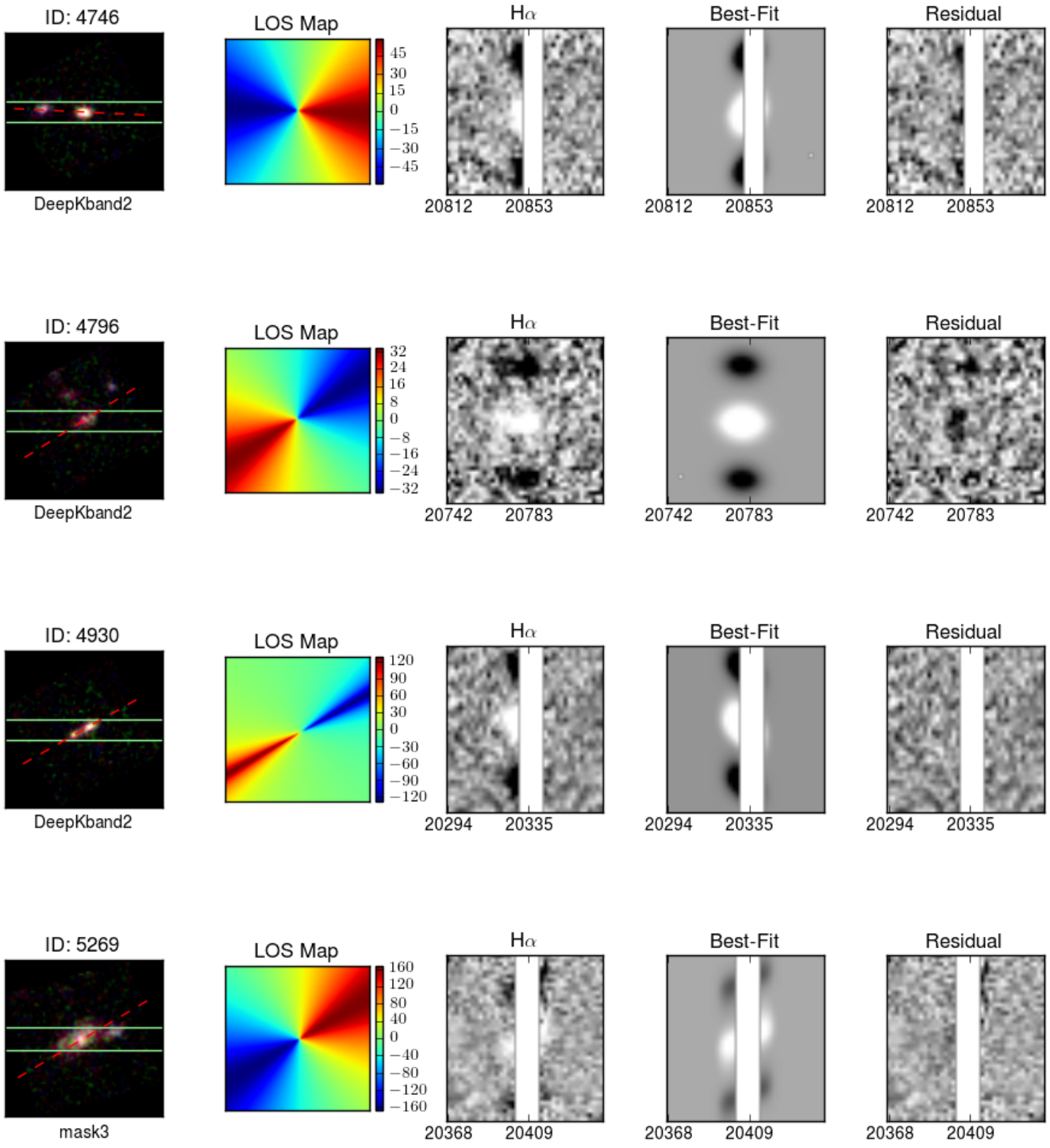

Figure 2. Continued

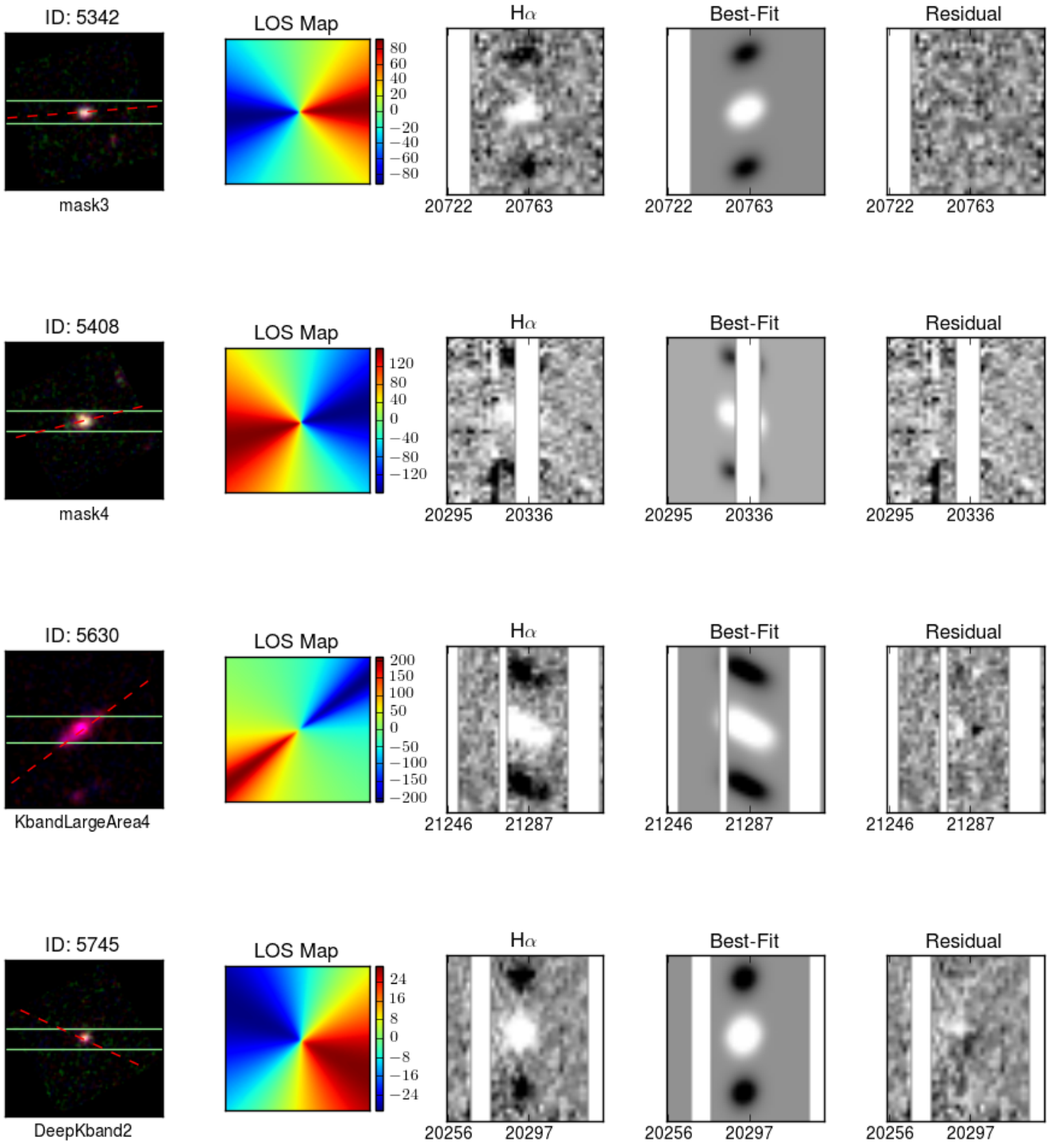

Figure 2. Continued

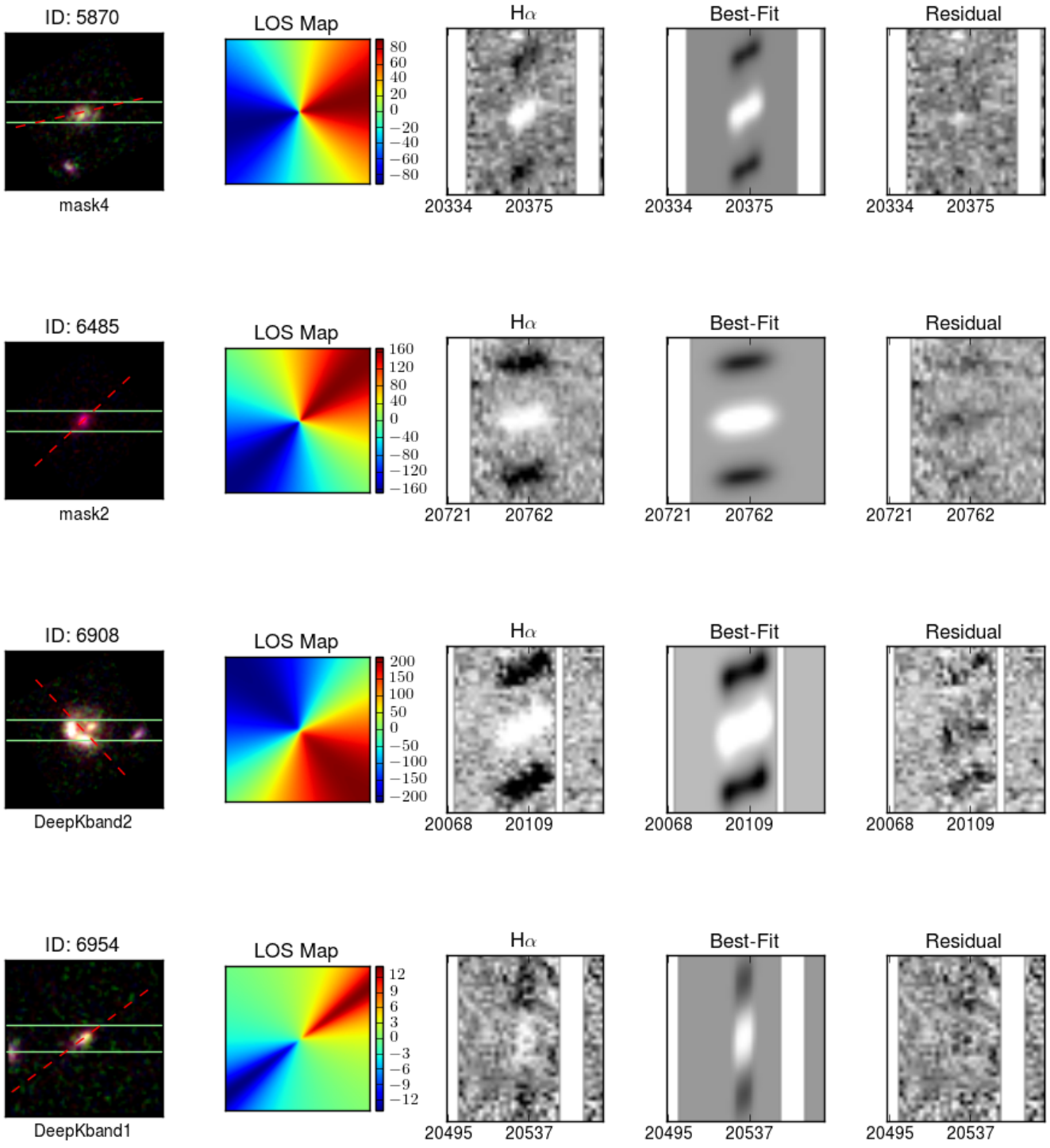

Figure 2. Continued

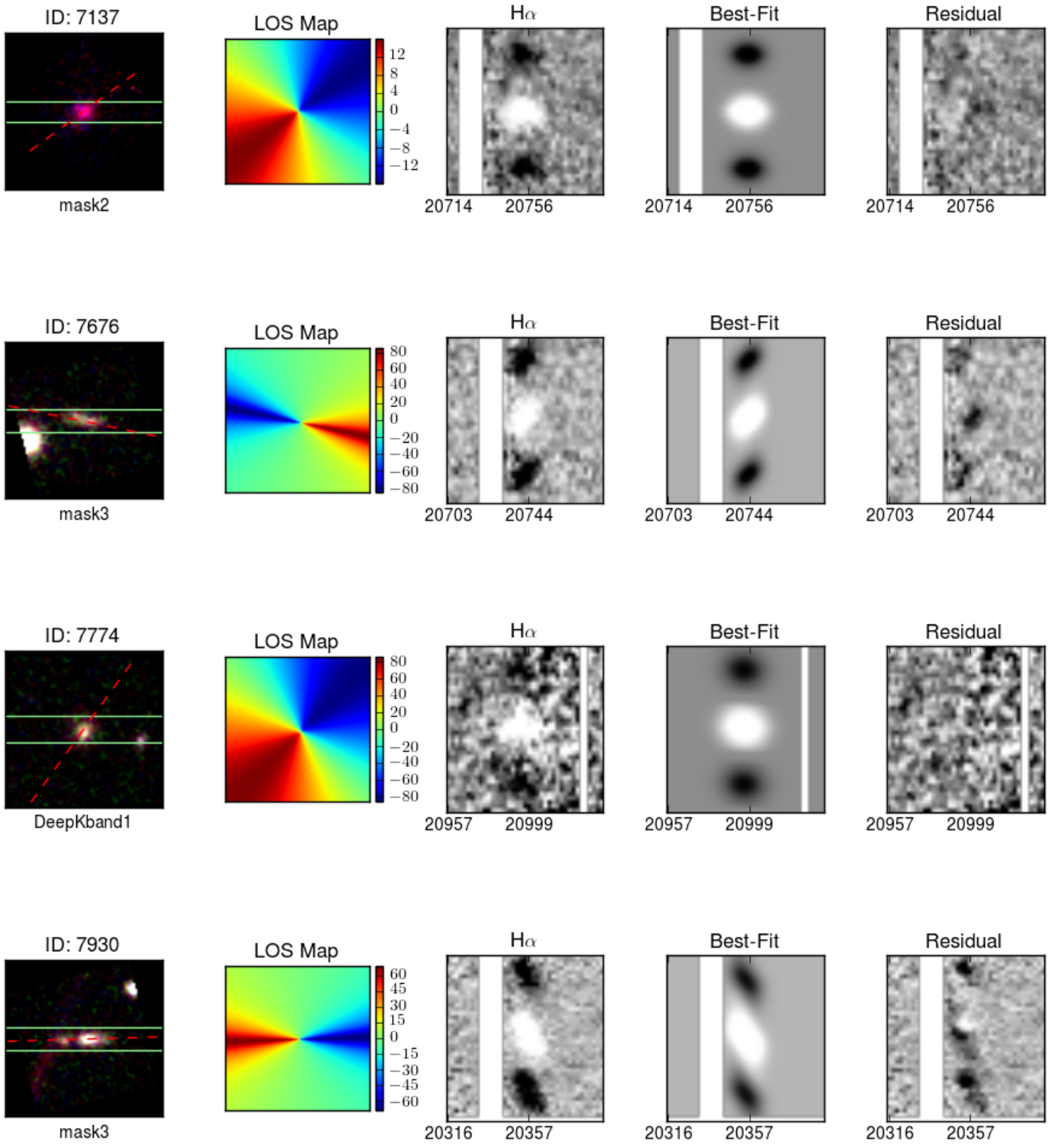

Figure 2. Continued

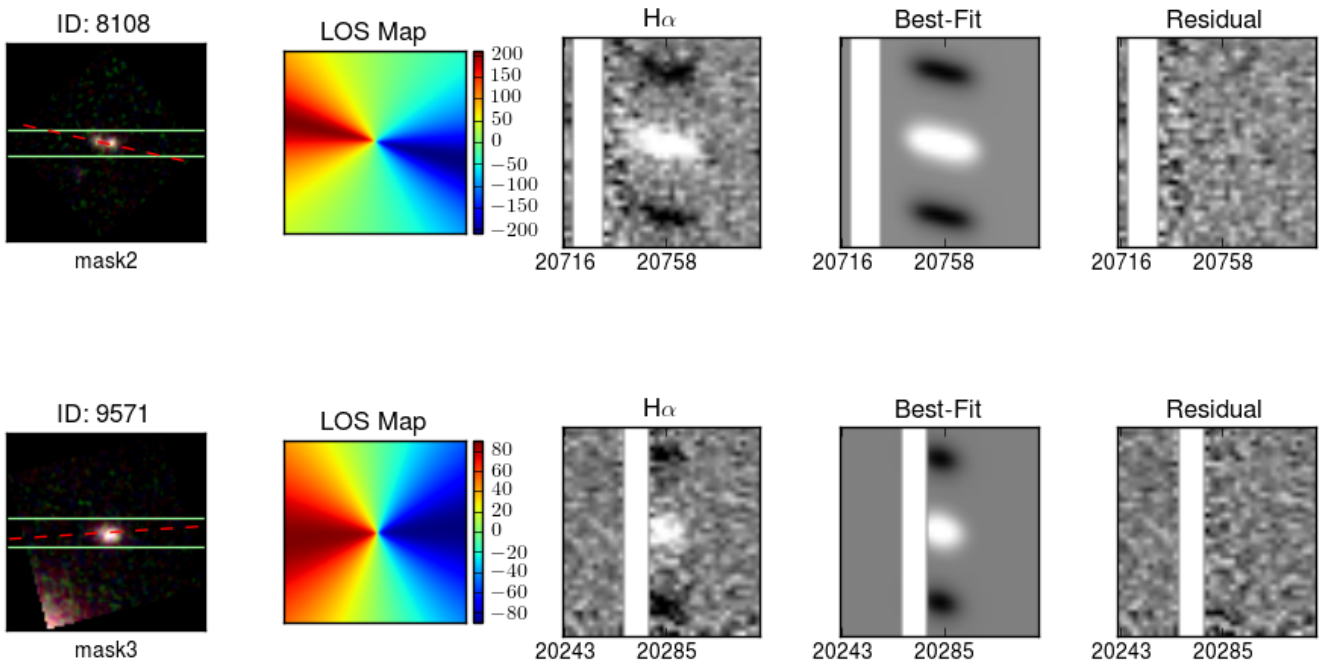

Figure 2. Continued

and $\beta = 2.5$. The values of these properties in our sample span the range of possible values in all cases, providing a diverse sample of disk galaxies, with $\frac{v}{\sigma} = 1 - 20$.

We measure pixel-to-pixel RMS from 2D MOSFIRE K-band observations and add simulated sky noise to each model (Figure 3). We do not simulate a continuum. Scale models to the sky noise to create mock observations at varying signal-to-noise (SNR) values (from SNR=5-60). If part of the line is masked from simulated sky emission, the SNR drops depending on the amount of line coverage. The SNR was calculated by summing all pixels of the spectrum within defined limits and dividing by the summed squares of the equivalent pixels in the corresponding noise spectrum. This region was defined as within $5r_s$ and $1.26''$ of the center of the object, and within $3FWHM$ of the emission line.

B.1. *The Effects of SNR and Masking Sky Emission*

When masking sky emission, we do not perform any operations on masked pixels. The fraction of pixels masked does affect recovery rates of our input models, and through our simulations we have found that if more than half of the emission line is masked at any SNR, we underestimate our input $V_{2.2}$ by 12% at half masked to 83% at 80 - 100% masked (Figure 4, Row 2, far right). Similar results are found in σ_g recovery: at 50% masked, we tend to overestimate σ_g by 20%, increasing to up to 70% overestimated at 80 - 100% masked (Figure 4, Row 4, far right). SNR correlates with recovery as well, although less significantly. At SNR > 10, we overestimate $V_{2.2}$ by $\sim 10\%$ at a 20% scatter, and at lower SNR we find the scatter to increase to $\sim$ 70% (Figure 4, Row 1, far right). For σ_g recovery, we find at SNR > 10, we tend to underestimate σ_g by 10% at a scatter of 15%, and at lower SNR the scatter can increase to $\sim$70% (Figure 4, Row 3, far right).

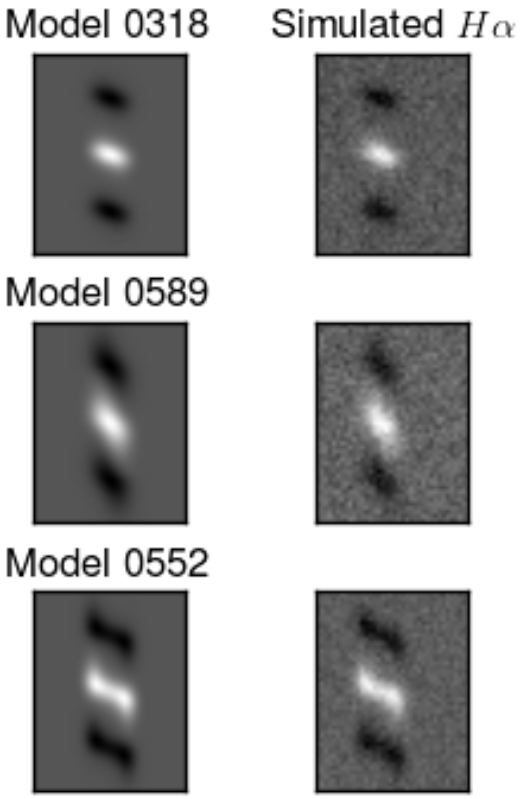

Figure 10. Examples of models used in our model library. Left column: Models from GBKFIT with 1.25″ dither patter. Right column: Models with low MOSFIRE-level sky noise added, with no sky emission. These are examples of our simulated observations, used to test the effectiveness of our method.

B.2. *Fixed and Free Turnover Radius*

The recovery of r_t is significant in the recovery of rotational velocity, as V_t is correlated with r_t. However, $V_{2.2}$ is a more reliable measurement due to a smaller offset from predicted. Similar surveys fix r_t in comparison to r_s e.g. $r_t = 0.4r_s$ (Price et al. 2015). We have decided our final sample will not hold r_t fixed, and instead will allow r_t to free values where $r_t < r_s$. However we include results if we fix $r_t = 0.33r_s$ and $r_t = 0.4r_s$ in our analysis.

In the case where we allow r_t to vary freely at any length below r_s, we find we overestimate r_t by around 30% of the input with a large scatter, while recovering our input r_s to a median offset of -20% of the input, and within a 1σ scatter of 15% of the input value. However we tend to overestimate our velocity at $r = 2.2r_s$, to within ∼10%. We recover σ_g to a small bias (∼10% underestimated from the input), at a 1σ scatter of 15%, increasing to 70% scatter at high line coverage and low SNR. Therefore, if we have bias in our results, we are overestimating the velocities in the $M_\star$-TFR and in $V_{2.2}/\sigma_g$. We also determine our ability to recover specific angular momentum, j_{disk} (underestimated by only ∼5% at low line coverage) and $V_{2.2}/\sigma_g$ (overestimated by 25% at low line coverage). Interestingly, the rotational velocity and the velocity dispersion are both recovered well below $r_s < 0.2''$. The size (both r_s and r_t) of the modeled galaxy seems to be uncorrelated with the recovery rate, possibly because all our modeled galaxies are smaller than the seeing they are convolved to.

In our simulated observations from GBKFIT, r_t is constantly held to be $r_s = 3r_t$. To determine our ability to recover the velocity, we try holding r_t to be at this fixed distance relative to r_s. When

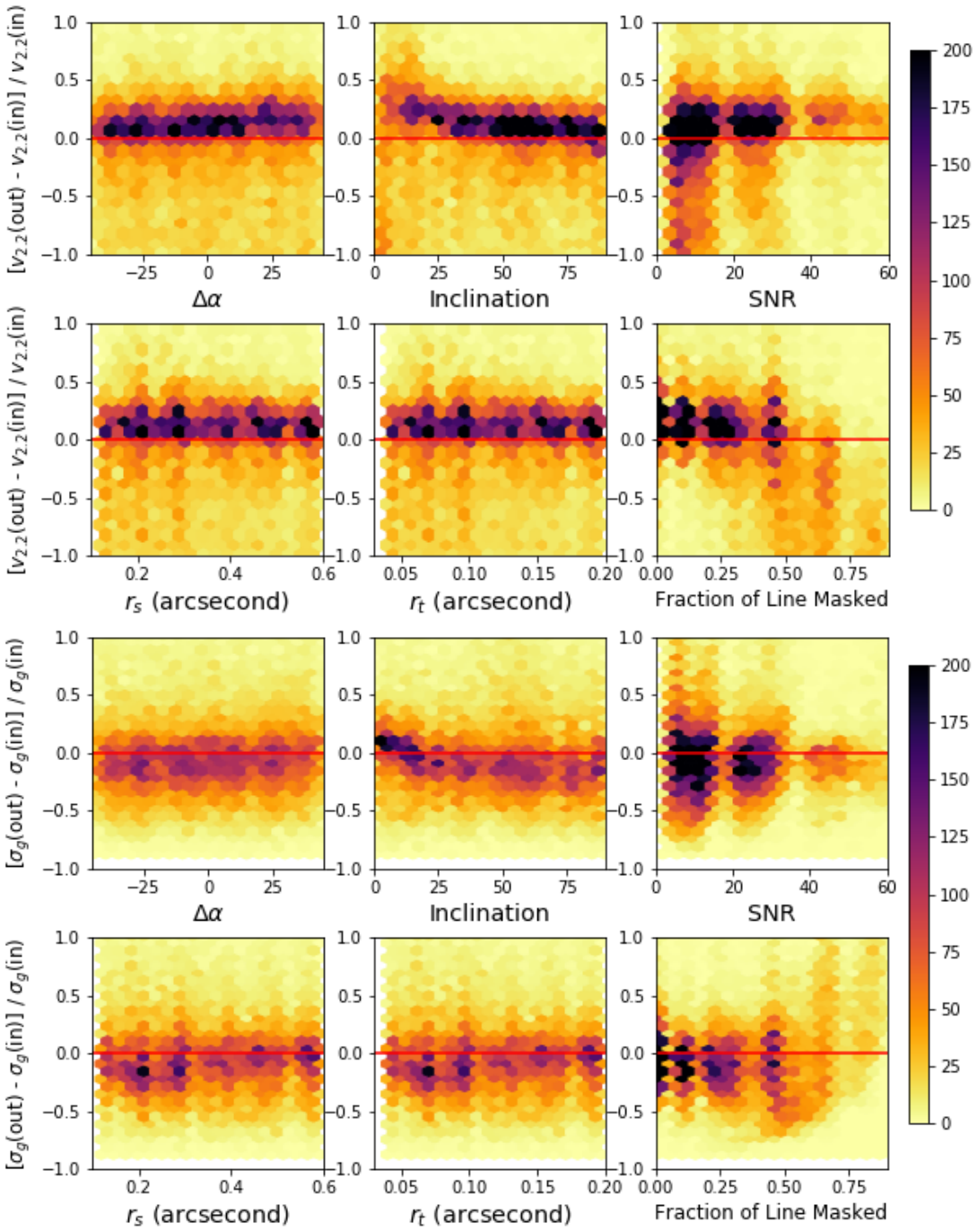

Figure 11. Recovery rates of $V_{2.2}$ and σ_g for simulated MOSFIRE observations at varying SNR and portion of the emission line masked (due to sky emission). Simulations are emission line models generated by GBKFIT, and embedded in MOSFIRE-level sky noise. Using HELA modeling, we test our recovery rate against (from left, top row) $\Delta\alpha$ (slit and morphological PA offset), inclination, SNR, (from left, bottom row) r_s (disk scale radius), r_t (turnover radius), and emission line masked fraction. All 2D histograms are plotted on the same color scale. We tend to overestimate $V_{2.2}$ by $\sim$10%, and underestimate σ_g by 10%. Inclination tends to have an effect at an inclination of 30^o, where we begin overestimating our $V_{2.2}$ by up to 30%. At more than half the emission line masked, our recovery is unreliable.

we recover our kinematic parameters while holding $r_t = 1/3r_s$, we find that we underestimate both r_t and r_s, but $V_{2.2}$ is recovered with only minor offsets (overestimated by $\sim$5% with a scatter of $\sim$20% at low line coverage). σ_g is still recovered at minor offsets (underestimated by 5%). j_{disk} is underestimated by 10% and $V_{2.2}/\sigma_g$ is overestimated by 25%. We find that we can reliably recover $V_{2.2}$ and σ_g at small offsets, as well as $S_{0.5}$ and j_{disk}. However, due to the small scatter in the recovered values for $V_{2.2}$ and σ_g, our $V_{2.2}/\sigma_g$ values have high scatter and are overestimated, and are thus likely unreliable.

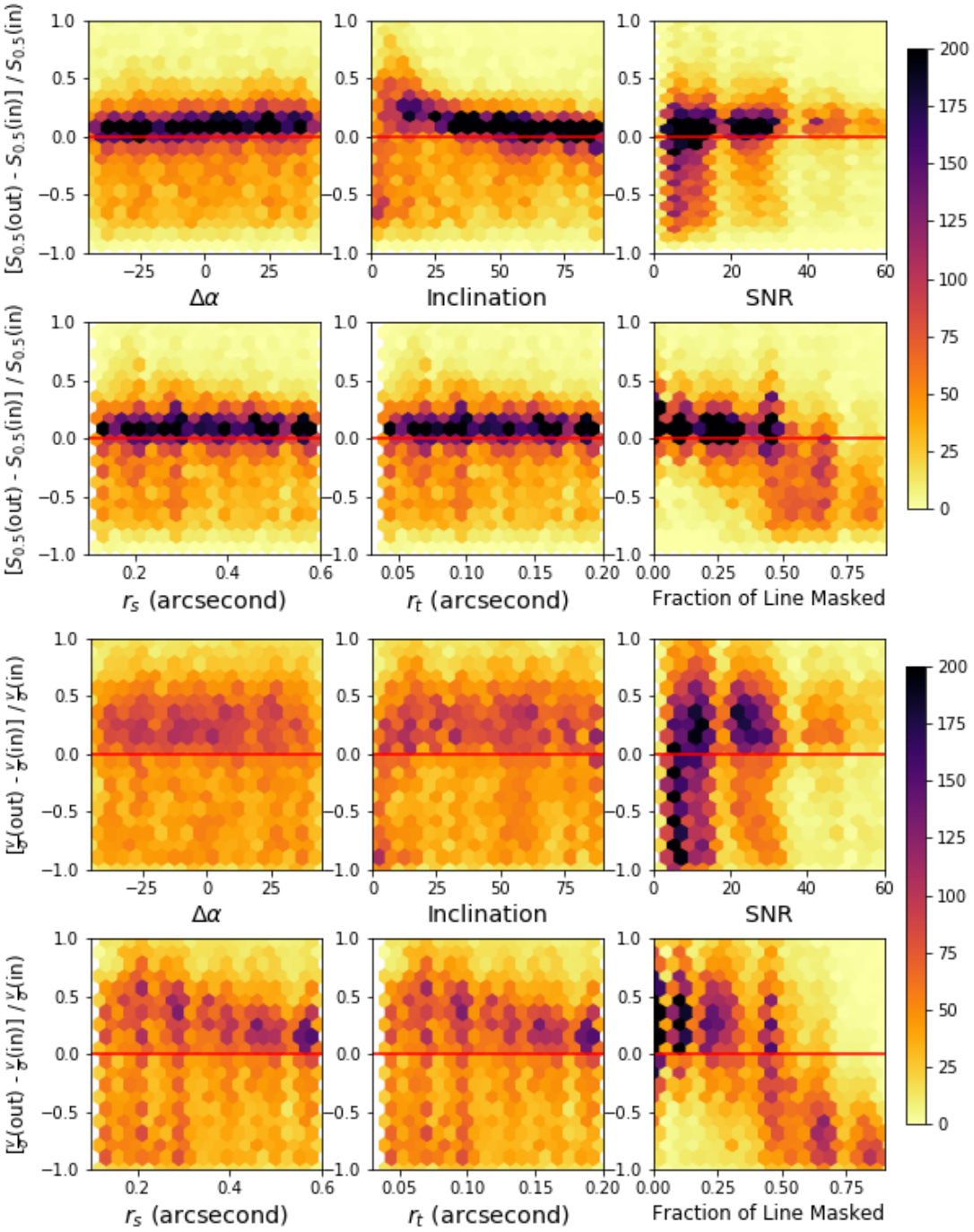

Figure 12. Recovery rates of $S_{0.5}$ and $V_{2.2}/\sigma_g$ for simulated MOSFIRE observations. Top: We overestimate $S_{0.5}$ by within 10% of the input values. Inclination affects recovery starting at around 30^o, where we begin overestimating $S_{0.5}$ by 20%. Bottom: $V_{2.2}/\sigma_g$ recovery is less reliable, where we tend to overestimate our values at around 25% of our input value with significant scatter. These results indicate that the $S_{0.5}$ parameter is by far the more reliable method of measuring kinematics, and $V_{2.2}/\sigma_g$ values are possibly biased too high and at high scatter.

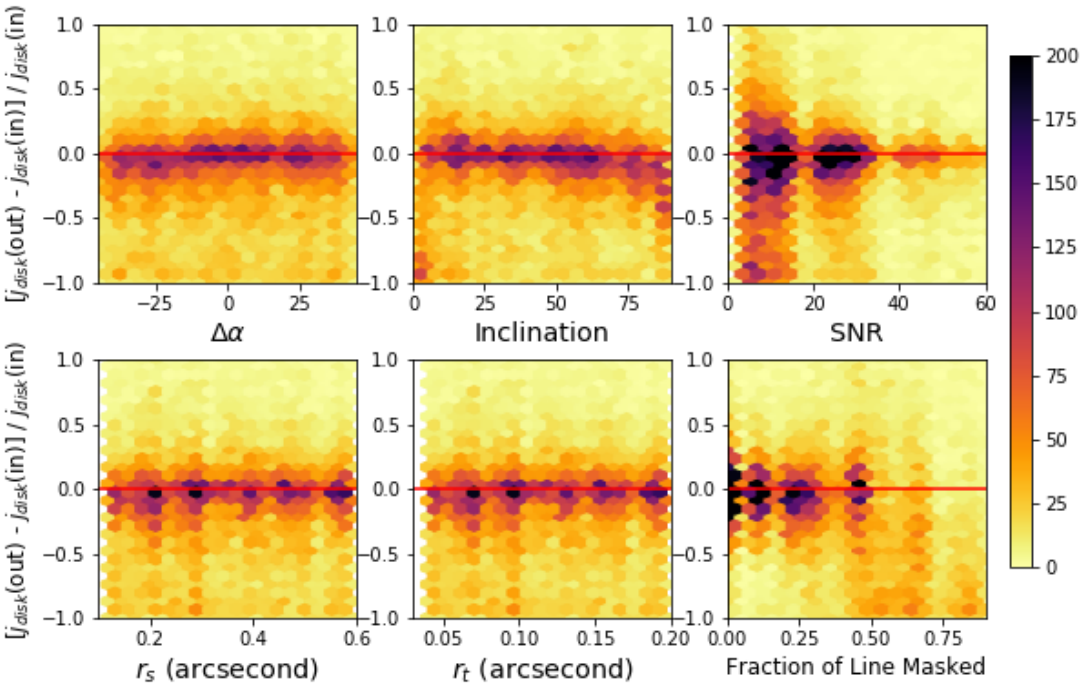

Figure 13. Recovery rate of j_{disk} for simulated MOSFIRE observations. We can reliably recover input j_{disk} for objects with less than 50% of the line masked, or with SNR>10.